

Further evidence for CCN aerosol concentrations determining the height of warm rain and ice initiation in convective clouds over the Amazon basin

5 *Ramon Campos Braga*¹, *Daniel Rosenfeld*², *Ralf Weigel*³, *Tina Jurkat*⁴, *Meinrat O. Andreae*^{5,9},
10 *Manfred Wendisch*⁶, *Ulrich Pöschl*⁵, *Christiane Voigt*^{3,4}, *Christoph Mahnke*^{3,8}, *Stephan Borrmann*^{3,8},
*Rachel I. Albrecht*⁷, *Sergej Molleker*⁸, *Daniel A. Vila*¹, *Luiz A. T. Machado*¹, and *Lucas Grulich*¹⁰

¹ Centro de Previsão de Tempo e Estudos Climáticos, Instituto Nacional de Pesquisas Espaciais, Cachoeira Paulista,
10 Brasil

² Institute of Earth Sciences, The Hebrew University of Jerusalem, Israel

³ Institut für Physik der Atmosphäre, Johannes Gutenberg-Universität, Mainz, Germany

⁴ Institut für Physik der Atmosphäre, Deutsches Zentrum für Luft- und Raumfahrt (DLR),
Oberpfaffenhofen, Germany

15 ⁵ Multiphase Chemistry and Biogeochemistry Departments, Max Planck Institute for Chemistry, 55020 Mainz, Germa-
ny.

⁶ Leipziger Institut für Meteorologie (LIM), Universität Leipzig, Stephanstr. 3, 04103 Leipzig, Deutschland

⁷ Instituto de Astronomia, Geofísica e Ciências Atmosféricas, Universidade de São Paulo, Sao Paulo, Brazil

⁸ Particle Chemistry Department, Max Planck Institute for Chemistry, 55020 Mainz, Germany.

20 ⁹ Scripps Institution of Oceanography, University of California San Diego, La Jolla, CA 92098, USA

¹⁰ Institut für Informatik, Johannes Gutenberg-Universität, Mainz, Germany

Correspondence to: Ramon C. Braga (ramonbraga87@gmail.com)

25

30

Abstract: We have investigated how aerosols affect the height above cloud base of rain and ice hydrometeor initiation and the subsequent vertical evolution of cloud droplet size and number concentrations in growing convective cumulus. For this purpose we used in-situ data of hydrometeor size distributions measured with instruments mounted on HALO aircraft during the ACRIDICON-CHUVA campaign over the Amazon during September 2014. The results show that the height of rain initiation by collision and coalescence processes (D_r , in units of meters above cloud base) is linearly correlated with the number concentration of droplets (N_d in cm^{-3}) nucleated at cloud base ($D_r \approx 5 \cdot N_d$). Additional cloud processes associated to D_r , such as GCCN, cloud and mixing with ambient air and other processes produce deviation of ~21% in the linear relationship, but it does not mask the clear relationship between D_r - N_d which was also found at different regions around the globe (e.g. Israel and India). When N_d exceeded values of about 1000 cm^{-3} , D_r became greater than 5000 m, and the first observed precipitation particles were ice hydrometeors. Therefore, no liquid water raindrops were observed within growing convective cumulus during polluted conditions. Furthermore, also the formation of ice particles took place at higher altitudes in the clouds in polluted conditions, because the resulting smaller cloud droplets froze at colder temperatures compared to the larger drops in the unpolluted cases. The measured vertical profiles of droplet effective radius (r_e) were close to those estimated by assuming adiabatic conditions (r_{ea}), supporting the hypothesis that the entrainment and mixing of air into convective clouds is nearly inhomogeneous. Additional CCN activation on aerosol particles from biomass burning and air pollution reduced r_e below r_{ea} , which further inhibited the formation of raindrops and ice particles and resulted in even higher altitudes for rain and ice initiation.

50 1. Introduction

Understanding cloud and precipitation forming processes and their impacts on the global energy budget and water cycle is crucial for meteorological modeling. Therefore, many studies have focused on improving cloud parameterization in numerical weather and climate models (e.g., Frey et al., 2011; Khain et al., 2005, 2000; Klein et al., 2009; Lee et al., 2007; Machado et al., 2014).

55 Cloud droplets form when humid air rises and becomes supersaturated with respect to water. Then water vapor condenses onto surfaces provided by pre-existing cloud condensation nuclei (CCN, a list of abbreviations and symbols is given in Table 1) aerosols. For ice formation, the ambient temperatures must reach values lower than $0 \text{ }^\circ\text{C}$. At temperatures between $0 \text{ }^\circ\text{C}$ and $-36 \text{ }^\circ\text{C}$, ice in convective clouds mostly forms inhomogeneously on ice nuclei (IN) aerosols, often when they interact with supercooled liquid water droplets (Pruppacher et al., 1998). Ice multiplication is an important mechanism that masks the primary ice nucleation activity when cloud droplets are sufficiently large to promote also warm rain by coalescence, at the temperatures of -3 to $-8 \text{ }^\circ\text{C}$ (Hallet and Mossop, 1974). At much colder temperatures (less than $-37 \text{ }^\circ\text{C}$), cloud particles freeze due to homogeneous ice nucleation (Rosenfeld and Woodley, 2000).

65 A cloud predominantly consists of droplets with diameters larger than about $3 \text{ }\mu\text{m}$, except for transient smaller sizes right at cloud base. The number concentration of cloud droplets (N_d in cm^{-3}) at cloud base mainly depends on the conditions below cloud base, i.e., the updraft wind speed (W) and the supersaturation (S) activation spectra of cloud condensation nuclei [$CCN(S)$] (Twomey, 1959). In very clean conditions, values of N_d near cloud base are in the range of ~ 50 - 100 cm^{-3} , while in polluted condition N_d may reach values between 1000 - 2000 cm^{-3} (Andreae, 2009; Rosenfeld et al., 2008, 2014a).

70 Below the freezing level, raindrops are formed due to cloud droplet coagulation (collision-coalescence) processes (warm rain process). Mixed phase precipitation results from interactions between ice particles and liquid water droplets (Pruppacher et al., 1998). Several studies based on aircraft, radar and satellite measurements support that warm rain

75 formation requires that the cloud consists of droplets with values of the effective radius (r_e) larger than 13-14 μm (Freud and Rosenfeld, 2012; Konwar et al., 2012; Prabha et al., 2011; Chen et al., 2008; VanZanten et al., 2005; Pinsky and Khain, 2002; Gerber, 1996; Rosenfeld and Gutman, 1994).

80 The effects of aerosol particles on clouds and precipitation have been studied in different parts of the globe (e.g., Fan et al., 2014; Li et al., 2011; Ramanathan et al., 2001; Rosenfeld and Woodley, 2000; Rosenfeld et al., 2014a; Tao et al., 2012; Voigt et al., 2017; Wendisch et al., 2016). A particularly interesting region is the Amazon basin, which presents contrasting environments of aerosol particle concentration between dry and wet seasons as well as steep aerosol
85 concentration gradients within regions with near-constant thermodynamic conditions (Andreae et al., 2004; Artaxo et al., 2013). The background number concentrations of aerosol particles and CCN over the pristine parts of the Amazon region are about a factor of 10 times lower than those of polluted continental regions, including polluted conditions over the Amazon (Martin et al., 2016). During the dry-to-wet transition season in the Amazon region, total aerosol number concentrations reach values up to 10,000 cm^{-3} , mostly due to forest fires (Andreae, 2009; Andreae et al., 2012; Artaxo et al., 2002). On the other hand, in the rainy season aerosol number concentrations are about 500-1000 cm^{-3} with CCN concentrations on the order of 200-300 cm^{-3} for 1 % supersaturation, mainly consisting of forest biogenic aerosol particles (Artaxo, 2002; Martin et al., 2016; Pöhlker et al., 2016; Pöschl et al., 2010). Additionally, Manaus city, which is located at the central Amazon basin, releases significant concentrations of urban pollution aerosol particles (e.g., due to traffic, combustion-derived particles, or different types of industrial activities). This increases CCN concentrations by
90 up to one order of magnitude (for 0.6% supersaturation) from the wet (Green Ocean) to the dry season (Kuhn et al., 2010).

Rosenfeld et al. (2012b) showed that by estimating the adiabatic number of droplets nucleated at cloud base (N_a), the height above cloud base at which the first raindrops evolve can be parameterized. This approach is based on the assumption that the entrainment and mixing of air into convective clouds is almost completely inhomogeneous (Beals et al., 2015; Burnet and Brenguier, 2007; Freud et al., 2011; Paluch, 1979). The inhomogeneous mixing occurs when evaporation rate of cloud droplets exceeds significantly the mixing rate of the cloud with ambient air. This causes the droplets that are at the boundary of the entrained air filament to evaporate completely and moisten that air until it is saturated. Further mixing of the saturated entrained air would not cause additional evaporation, but only decreasing of N_a and LWC, while maintaining r_e of the remaining droplets unaffected. This implies that the vertical profile of the actual cloud droplet effective radius behaves nearly as in an idealized adiabatic cloud. This connects uniquely the adiabatic drop number concentration, which is approximated by N_a at cloud base, with the adiabatic droplet effective radius (r_{ea}), based on an adiabatic parcel model for which droplet growth is dominated by condensation (Freud and Rosenfeld, 2012; Pinsky and Khain, 2002). This parameterization can be applied to estimate the height above cloud base at which raindrops start to form, when r_{ea} reaches 13 μm (D_{13}) [Freud and Rosenfeld, 2012; Konwar et al., 2012; Rosenfeld et al., 2012b; Prabha et al., 2011; VanZanten et al., 2005]. However, uncertainties associated to the calculated N_a decrease the agreement between r_{ea} and r_e . Most of these uncertainties arise when additional CCN activation of droplets happens above cloud base because the adiabatic model does not predict that N_a increases with height, but decrease due to evaporation and deviations from inhomogeneous cloud mixing (Pinsky and Khain, 2012).
100

110 Braga et al. (2017) applied the methodology described by Freud et al. (2011) to calculate N_a at the base of growing convective cumulus clouds for the Amazon region during the ACRIDICON-CHUVA (Aerosol, Cloud, Precipitation, and Radiation Interactions and Dynamics of Convective Cloud Systems)-CHUVA (Cloud processes of the main precipitation systems in Brazil: A contribution to cloud resolving modeling and to the GPM [Global Precipitation Measurements]) campaign (Wendisch et al., 2016). The N_a is calculated from $N_a = CWC_a / M_{va}$, where CWC_a is the adiabatic cloud water content (CWC_a) as calculated from cloud base pressure and temperature, and M_{va} is the adiabatic mean

115 volume droplet mass, as approximated from the actually measured mean volume droplet mass (M_v) by the cloud probe
DSDs obtained during the cloud profiling measurements. Measurements of M_v with height are considered only for cloud
passes where CWC is greater than 25 % of the adiabatic CWC and r_e is lower than 11 μm (i.e. for cloud droplets which
have grown mostly via condensation). The calculated N_a based on the measured vertical profile of r_e agreed well (within
20-30 %) with the actual measurements of cloud droplet number concentrations at cloud base. This approach provides
120 the opportunity to test the agreement between estimated r_{ea} and the height above cloud base of warm rain initiation (D_r)
within clouds for the Amazon region. In addition, measurements of the height above cloud base of ice initiation (D_i) in
convective clouds are also available from flights that include cloud penetrations at ambient temperatures as low as -60
°C with the HALO aircraft (Wendisch et al., 2016).

This study analyzes the vertical development of cloud and precipitation particles (water drops and ice crystals) in
125 growing convective cumulus over the Amazon, based on measurements of cloud microphysical properties from
instruments mounted on HALO during ACRIDICON-CHUVA (Wendisch et al., 2016). The vertical profile of r_{ea} is used
to estimate the depth above cloud base at which warm rain initiation occurs. The dominance of inhomogeneous mixing
causes the r_e profile to behave almost as in adiabatic clouds, constrained by N_d at cloud base (Burnet and Brenguier,
2007; Freud et al., 2011). This means that the height above cloud base for reaching r_e of 13-14 μm , which is required for
rain initiation, is also determined by cloud base N_d (Freud and Rosenfeld, 2012). Rain initiation depends strongly on r_e
130 because the rain production rate by collision and coalescence is proportional to $\sim r_e^5$ (Freud and Rosenfeld, 2012). Here
we test and quantify these relationships for the measurements conducted with HALO aircraft during ACRIDICON-
CHUVA.

The HALO flights during the ACRIDICON-CHUVA campaign were performed over the Amazon region under various
135 conditions of aerosol concentrations and land cover (Wendisch et al., 2016). Figure 1a shows the flight tracks during
which cloud profile sampling in growing convective cumulus was performed. Figure 1b shows a schematic sketch of
the flight pattern while sampling cloud clusters (the locations in three dimensions of each flight are available at Figure 1
on supplementary material). The aircraft obtained a composite vertical profile by penetrating young and rising convec-
tive elements, typically some 100-300 m below their tops.

140 The cloud droplet size distributions (DSDs) between 3-50 μm diameter were measured at a temporal resolution of 1
second by the CAS-DPOL and CCP-CDP probes (Baumgardner et al., 2001; Lance et al., 2010; Brenguier et al., 2013).
Each DSD spectrum represents 1 s of flight path (covering ~ 150 m of horizontal distance for a typical aircraft speed).
The value of r_e was calculated for each 1-s DSD. The two probes (CAS-DPOL and CCP-CDP) were mounted on
opposite wings of HALO (horizontal distance of ~ 15 m). Similar values of N_d and derived r_e were measured by CAS-
145 DPOL and CCP-CDP (they agree within 30 %), even though they were mounted on different wings. A previous study
(Braga et al, 2017) showed that both probes were in agreement within the measurement uncertainties with respect to the
measured cloud droplet number concentrations at cloud base and in accordance with the expected values for different
conditions of CCN concentration and updraft wind speed below cloud base. In addition, the CWC calculated from the
measured DSDs shows similar values to those measured with a hot wire device for different heights above cloud base
150 [the probes' measurements agree within their uncertainty range (16% for probe DSDs and 30% for hot-wire device)]
(Braga et al., 2017).

The determination of the height of rain initiation is based on the drizzle water content (DWC) calculation from the
CCP-CIP probe (Brenguier et al., 2013). The DWC is defined as the mass of the drops integrated over the diameter
range of 75–250 μm (Freud and Rosenfeld, 2012). This size range is selected because it includes only drops with
155 terminal fall speed of 1 m s^{-1} or less, which maximizes the chance that the drizzle was formed *in situ* and did not fall a

large distance from above. Rainwater content (RWC) is defined as the CCP-CIP integrated liquid water mass of droplets with diameters between 250 and 960 μm . The CCP-CIP images were used to distinguish raindrops and ice particles during cloud passes. The hydrometeor type is identified visually by their shapes. The phase of the smaller CCP-CIP particles cannot be distinguished. Therefore, the precipitation is considered as mixed phase when ice particles are identified, and the combined DWC and RWC are redefined as mixed phase water content (MPWC). Table 2 summarizes the calculated cloud microphysical properties with respect to the instrumentation used and its size ranges.

2. The scientific motivation

The aircraft based *in situ* measurements of cloud properties were collected within convective clouds formed over the Amazon from cloud base up to cloud top above the glaciated level. These measurements provided a unique opportunity to evaluate previous theoretical knowledge about aerosol impacts on convective clouds characteristics over the Amazon. In this study the impact of N_a (adiabatic cloud drop concentrations) in determining the initiation of rain and ice within convective clouds is evaluated. This is performed through the analysis between the calculated N_a , D_r and D_i for several different environmental conditions over the Amazon (cloud base updrafts, aerosol concentration, surface cover etc.). The relationship of N_a and D_r was previously analyzed for regions of Israel and India where a linear relationship was found ($D_r \approx 4 \cdot N_a$) [Freud and Rosenfeld, 2012]. For Amazon region a similar analysis is performed here also taking in account the impact of N_a in D_i . This is the first study which analyzes the impact of N_a on D_r and D_i at Amazon region using *in situ* measurements of convective cloud properties. The results obtained from comparisons of N_a estimates and the measured effective number of droplets nucleated at cloud base (N_a^*), shown at Braga et al. (2017) for the same flights in the Amazon region, support the methodology of deriving N_a based on the rate of r_e growth with cloud depth, and under the assumption that the entrainment and mixing of air into convective clouds is extremely inhomogeneous. This is important because the characteristics of convective clouds based on N_a values can be extended in space and time by their application to satellite-calculated N_a (which is obtained with the same parameterization that has been recently developed from the satellite-retrieved vertical evolution of r_e in convective clouds) [Rosenfeld et al., 2014b].

3. Instrumentation

3.1 Cloud particle measurements

The instrumentation used to measure cloud particles and rain or ice formation consists of three cloud probes: CAS-DPOL, CCP-CDP and CCP-CIP (Brennguier et al., 2013). In this study, cloud particle counts are accumulated for bin diameters larger than 3 μm from the CCP-CDP and CAS-DPOL; the lower size bins from these probes overlap with haze particles. Nucleated cloud drops in convective clouds grow quickly beyond 3 μm . Details about the cloud probe measurements characteristics are described in the following sub-sections and in Braga et al. (2017).

3.2.1 CCP-CDP and CCP-CIP measurements

The Cloud Combination Probe (CCP) combines two detectors, the Cloud Droplet Probe (CDP) and the greyscale Cloud Imaging Probe (CIPs). The CDP detects forward scattered laser light of cloud particles when penetrating the CDP detection area (Lance et al., 2010). The CIP records 2-D shadow cast images of cloud elements. In this study, we deduced the existence of ice from the occurrence of visually non-spherical shapes of the shadows. The particle detection size range is 2 μm to 960 μm when measuring with the CCP at 1 Hz frequency (Wendisch et al., 2016). The combination of CCP-CDP and CCP-CIP information provides the ability to measure cloud droplets and raindrops within clouds for nearly the same air sample volume. The maximum number of particles measured by CCP-CDP and CCP-CIP

are about 2,000 and 500 cm⁻³ for 1 Hz cloud pass, respectively. For the data processing of the CIP measurements, ice is assumed as the predominant particle phase in the mixed-state cloud conditions throughout the ACRIDICON-CHUVA campaign. The assumption of ice density instead of water density implies a slight overestimation (~10 %) of the calculated rain water content for particles greater than 75 μm. An additional data processing assuming water density as the predominant particle phase was performed for flights which warm rain was initiated below the 0 °C isotherm.

3.2.2 CAS-DPOL measurements

The CAS-DPOL measures particle size distributions between 0.5 and 50 μm at 1Hz time resolution (Baumgardner et al., 2011; Voigt et al., 2010; Voigt et al., 2011). Number concentrations are derived using the probe air speed measured at the instrument. Particle inter-arrival time analysis did not show influences of coincidence (Lance, 2012). The data analysis and uncertainties are described in detail in Braga et al. (2017).

Braga et al. (2017) have shown sufficient agreement between both CAS-DPOL and CCP-CDP measurements of cloud droplet number concentration to distinguish convective clouds that develop above clean vs. polluted regions during the ACRIDICON-CHUVA campaign. In addition, the CWC estimated by integration of the DSDs measured with both probes showed good agreement with hot wire CWC measurements (Braga et al., 2017).

3.3 Meteorological data

The HALO aircraft was equipped with a meteorological sensor system (BASIC HALO Measurement And Sensor System - BAHAMAS) located at the nose of the aircraft (Wendisch et al., 2016). The uncertainties for measurements of temperature, relative humidity and vertical wind speed are 0.5 K, 5 % and 0.3 m s⁻¹, respectively (Mallaun et al., 2015).

3.4 Aerosol measurements

Aerosol particle measurements were performed using the Passive Cavity Aerosol Spectrometer Probe 100X (PCASP-100X), which is an airborne optical spectrometer that measures aerosol particles in the 0.1 μm to 3 μm diameter range (Liu et al., 1992). The maximum number of particles measured by PCASP is about 3,000 cm⁻³ for 1 Hz cloud pass. During ACRIDICON-CHUVA campaign PCASP was not operated with a heated inlet, thus, the measured aerosol particles below cloud base (about 200 m) can be larger than the original dry size due to swelling.

4. Methods

The analyses are performed along the following general steps:

- a) The relationship between r_e and the probability of drizzle is found. The value of r_e is calculated from the size distributions measured by the CAS-DPOL and the CCP-CDP (two different values). DWC, RWC, and MPWC are obtained from the CCP-CIP data. The calculations of these cloud properties are detailed at section 4.1.
- b) The N_a at cloud base is estimated through the vertical profile of r_e . The calculation of N_a is detailed at section 4.2.
- c) The height of rain initiation based on the modeled adiabatic growth of r_e with height is estimated for different aerosol condition as a function of estimated N_a . The value of D_{13} is estimated as the cloud depth for which the adiabatic r_e reaches 13 μm (as described also at section 4.2).
- d) The extent of agreement between the directly measured D_r within convective clouds and the estimated D_{13} based on the assumption of adiabatic r_e growth and on the measured r_e is discussed at sections 5 and 6.

4.1. Estimation of r_e , rain and ice initiation

240 Rain is initiated during the warm phase of growing convective cumulus by intensification of the collision and coalescence (coagulation) processes with height. The efficiency of the process of droplet coalescence is determined by the collection kernel (K) of the droplets and their concentrations (Pruppacher et al., 1998). Freud and Rosenfeld (2012) have shown through model simulations and aircraft measurements that $K \propto r_v^{4.8}$, where r_v is the mean volume radius obtained from the cloud probe DSDs in the absence of ice. r_v is defined as follows:

$$r_v = \left(\frac{3 \text{CWC}}{4 \pi \rho N_d} \right)^{\frac{1}{3}} \quad (1)$$

245 where ρ is the water density (1 g cm^{-3}), CWC is in g m^{-3} , and N_d is in cm^{-3} . The values are obtained from the 1-Hz data of droplet size distributions from the cloud probes. The calculation of CWC is performed separately with CAS-DPOL and CCP-CDP probe droplet concentrations as follows:

$$250 \quad \text{CWC} = \frac{4\pi}{3} \rho \int N(r) r^3 dr \quad (2)$$

where N is the droplet concentration and r the droplet radius. The calculations of DWC, RWC, and MPWC are done in similar fashion to CWC but with different cloud probes and particle size ranges (see Table 2).

The definition of r_e is:

$$255 \quad r_e = \frac{\int N(r) r^3 dr}{\int N(r) r^2 dr} \quad (3)$$

Freud and Rosenfeld (2012) showed that $r_v \approx 1.08 \cdot r_e$, depending on the droplet size distribution. Using this relationship, they derived r_e from r_v and showed that warm rain initiates within clouds when r_e is about 13-14 μm (Klein et al., 2009; Rosenfeld and Gutman, 1994; Rosenfeld and Lensky, 1998; Rosenfeld et al., 2012a, 2014c).

260 Only measurements with CWC larger than 25% of the adiabatic water content are considered in order to exclude convectively diluted or dissipating clouds. It is assumed that rain (or ice) formation starts when calculated DWC exceeds 0.01 g m^{-3} (Freud and Rosenfeld, 2012). For rain initiation in liquid phase the DWC threshold is $\sim 10\%$ greater due to the overestimation of DWC during CIP measurements in warm clouds (as stated at Section 3.2.1). The small terminal fall speed of the drizzle drops ($\leq 1 \text{ m s}^{-1}$) allows to focus on in-situ rain (or ice) initiation while minimizing the amount of DSDs affected by rain drops fallen from above into the region of measurements. In addition, cloud passes with rain were eliminated when cloud tops were visibly much higher than the penetration level ($> \sim 1000 \text{ m}$), based on the videos recorded by the HALO's cockpit forward-looking camera. However, cloud tops higher than few hundred meters above the penetration level occurred only rarely.

265 Table 3 shows the cloud depth above cloud base at which warm rain initiation (D_r) occurs (i.e., $\text{DWC} > 0.01 \text{ g m}^{-3}$) for all flights as a function of estimated N_d . The D_r is taken as the cloud depth for ice initiation (D_i) if ice particles are evident in the CCP-CIP images. Here, the D_i is visually ascribed for sizes greater than $\sim 0.25 \text{ mm}$ and it does not mean that frozen smaller particles cannot be present. The assumption of water or ice density as the predominant particle phase on DWC calculation based on CCP-CIP probe did not impact D_r and D_i measured because the DWC threshold (i.e., $\text{DWC} > 0.01 \text{ g m}^{-3}$) for warm rain or ice initiation was achieved at the same cloud depth for both particles densities. Additional details about the cloud profiling characteristics for each flight as the number of altitude levels sampled
275 (NLS), highest cloud depth without raindrop ($D_{r,l}$) or ice particles ($D_{i,l}$) etc. are also available in Table 3. Furthermore, Appendix A discusses the uncertainty calculations of the estimated parameters of cloud properties.

4.2. Estimating N_a and adiabatic r_e

The N_a for the convective clusters is estimated based on the slope between the calculated adiabatic CWC (CWC_a) and the mean volume mass of the droplets (M_v), which is the mass of a water sphere having the radius r_v . M_v is calculated for 1-s DSD measurements of CAS-DPOL and CCP-CDP for non-precipitating cloud passes (Braga et al., 2017). The underlying assumption is that the measured r_v is approximating the adiabatic r_v (r_{va}) due to the nearly inhomogeneous mixing behavior of the clouds with the ambient air (Beals et al., 2015). Therefore, the measured M_v approximates the adiabatic M_v (M_{va} , where $M_{va} = CWC_a / N_a$). This methodology does not account for cloud mixing losses from droplet evaporation of additional drop activation. Both incur an overestimation of N_a . It was found that the calculated N_a based on the vertical profile of r_e commonly overestimate the measured N_a near cloud base by 30 % (Freud et al., 2011). Therefore, in calculating N_a a factor of 0.7 is applied to N_a estimates. Braga et al. (2017) have shown that this estimated N_a was in a reasonably good agreement with the directly measured cloud base droplet number concentration, N_d , as obtained from the CCP-CDP and CAS-DPOL during ACRIDICON-CHUVA. Once N_a is estimated, the adiabatic r_e (r_{ea}) can be calculated based on a simple adiabatic parcel model where droplet growth is dominated by condensation (Pinsky and Khain, 2002), where $r_{ea} = 1.08 \cdot r_{va}$. The value of D_{13} is defined as the cloud depth for which r_{ea} reaches 13 μm . The uncertainties calculations of cloud properties estimated from cloud probes were described in Braga et al. (2017). The uncertainties of r_e , r_v , r_{ea} , r_{va} are about 10%, while for CWC and M_v the uncertainties are about 30%. The N_a calculation does not take into account the possibility of new nucleation above cloud base (Freud et al., 2011). Braga et al. (2017) have shown that the assumption of adiabatic growth of droplets via condensation from cloud base to higher levels within cloud can lead to an overestimation by ~20-30% of the number of droplets at cloud base when calculating N_a in cases with additional droplet nucleation above cloud base.

The N_a calculated for cloud base was used to classify clouds as having developed in clean, polluted, or very polluted regions. A clean cloud case was defined as $N_a < 500 \text{ cm}^{-3}$, polluted for $500 \text{ cm}^{-3} < N_a < 900 \text{ cm}^{-3}$, and very polluted for $N_a > 900 \text{ cm}^{-3}$. During ACRIDICON-CHUVA, a flight in clean clouds (AC19) was performed over the Atlantic Ocean. Clouds observed during flights over the northern Amazon were classified as polluted, mainly due to diluted smoke from biomass burning advected by long-range transport. This region represents the Amazon background condition for aerosol concentration during the dry season. Very polluted conditions were met over the Central Amazon, which was affected strongly by biomass burning over the Amazonian deforestation arc (southern Amazon).

305

5. Results

5.1 Threshold of r_e for warm rain initiation

The values of r_e derived from integrating the cloud probe DSDs were used to identify rain initiation. Some caution is required to eliminate possible bias resulting from peculiar shapes of the drop size spectrum. An r_e value of 13-14 μm represents the rain initiation threshold for growing convective cumulus observed at different locations in the world, as long as there is no significant influence from giant CCN (GCCN; dry soluble diameter $> 1 \mu\text{m}$) (Freud and Rosenfeld, 2012). The presence of GCCN during cloud droplet formation at cloud base can lead to a faster formation of raindrops due to both, the rain embryo effect and the competition effect that reduces cloud base maximum supersaturation and consequently reduces N_d (Rosenfeld, 2000; Segal et al., 2007). Such cases are very common over the ocean due to sea spray aerosols; there, the values of r_e at which raindrops start to form are commonly smaller than the usual threshold of 13-14 μm (Freud and Rosenfeld, 2012). In our study the DSDs from flight AC19 performed over the Atlantic Ocean did not show a large drop tail near cloud base (see Figure 2 in the supplementary material). The cumulative sample volume

315

from CCP-CDP probe at cloud base was about 5.8 L^{-1} for 176 s of measurements. The figure shows the scarcity of large cloud droplet (with diameters $> 20 \text{ }\mu\text{m}$) near cloud base, where the mean concentration of such droplets is smaller than 0.1 drop cm^{-3} . Such small concentration of large droplets at cloud base is insufficient to have any significant effect on supersaturation.

Figures 2a-b show the precipitation initiation probability as a function of r_e calculated from the CCP-CDP and CAS-DPOL probes for all flights analyzed over the Amazon. The probability of precipitation is the fraction of 1-Hz in-cloud measurements which exceed certain DWC thresholds (i.e. for $\text{DWC} > 0.01 \text{ g m}^{-3}$). This was done as a function of r_e value. These figures show that for the CCP-CDP probe rain initiation is expected to occur at $r_e > 13 \text{ }\mu\text{m}$, whilst for CAS-DPOL the rain initiation threshold is $r_e > 12 \text{ }\mu\text{m}$. Difference of the two instruments in the r_e range below $\sim 7 \text{ }\mu\text{m}$ and above $\sim 11 \text{ }\mu\text{m}$ have been discussed in Braga et al. (2017). For $r_e < 7 \text{ }\mu\text{m}$, they are related to a higher sensitivity of the CAS-DPOL for small cloud and aerosol particles, whereas for $r_e > 11 \text{ }\mu\text{m}$ CAS-DPOL has lower sensitivity to large particles than CCP-CDP; however the differences are not significant within the uncertainties of the measurements. Because the CCP-CDP was mounted very close to the CCP-CIP, results from this probe are shown in subsequent sections; similar results were found from data collected with the CAS-DPOL probe.

5.2 Comparing estimated r_{ea} with measured r_e

The comparison between the values of r_{ea} (calculated from the estimated N_a at cloud base described in Section 4.2) with the measured r_e is the basis for analyzing the evolution of cloud particle size until rain or glaciation initiation occurs within the cloud. Rosenfeld et al. (2012b) showed that a tight relationship between the N_a calculated for cloud base and the evolution of r_{ea} with height ($r_{ea}-D_c$) provides a useful proxy of the depth in convective clouds at which raindrops start to form.

5.2.1 Case study: Flight AC07 over the Amazon deforestation arc

Flight AC07 was performed over the deforestation arc (see Figure 1a). Figure 3 shows the number of droplets measured at different heights in the convective clouds. Droplet concentrations reaching $\sim 2000 \text{ cm}^{-3}$ were measured at cloud base, which is characteristic for very polluted clouds. The cloud base was located at about 1900 m above sea level, with ambient air temperature at about 15°C . Figure 4a shows the mean DSD for a cloud penetration at cloud base. It emphasizes the higher number concentration of small droplets ($< 10 \text{ }\mu\text{m}$) that are observed in convective clouds forming in polluted environments. Figure 4b shows the evolution of r_e measurements and estimated r_{ea} as a function of temperature. The figure also shows that the values of r_e do not exceed the $13 \text{ }\mu\text{m}$ threshold at warm temperatures. These results suggest that cloud droplets formed at cloud base grow mainly via condensation and no raindrops were formed during the warm phase of convective cloud development. However, to rule out coalescence processes as a possible reason for droplet growth, further analysis using CCP-CIP images was done.

Figures 5a-c show the evolution of DSD and CWC (mean values) as a function of height above cloud base and the cloud particle images from the CCP-CIP. Figure 5a plots the data for a cloud pass at warm temperatures and Figures 5b-c result from measurements during cloud passes at cold temperatures. The DSDs show that most droplets have a diameter smaller than $20 \text{ }\mu\text{m}$, and only very few large droplets are observed for warm temperatures. The CCP-CIP detected only cloud droplets and no raindrops, as evident by both RWC and $\text{DWC} < 0.01 \text{ gm}^{-3}$. At cold temperatures, the CCP-CIP images show the irregular shapes of large ice particles. No spherical raindrop shapes were found in these data for any of the cloud passes, including those collected at warm temperatures. The DWC and RWC calculated from the mean DSDs show values greater than zero only when ice particles were observed on the CCP-CIP images. Also, for a cumulative sample volume of 1.24 m^{-3} from 89 s of CCP-CIP measurements, no raindrop were observed between the

360 heights above cloud base of 2,900 m (0°C) and 7,100 m (-26.25 °C). This means that the raindrop concentration, if any, was smaller than 1 drop m⁻³. This is a negligible rain rate, and supports the notion of practical shut of coalescence. Furthermore, the CCP-CIP did not detect any raindrops at lower levels (warm temperatures) for a cumulative sample volume of 5.9 m⁻³ from 426 s of measurements. These results indicate a strong inhibition of raindrop formation within growing convective cumulus for this flight over the deforestation arc of the Amazon. Even though some of the indicated
365 effective radii values are larger than 13 μm for colder temperatures, these values do not indicate rain formation when only ice particles are observed. This does not exclude the possibility that small raindrops froze soon after their formation in such low temperatures.

The mean DSD and CIP images shown in Figure 5c result from a passage through a convective cloud with lightning activity. Figure 6 shows a photo of the cloud taken from the HALO cockpit just before the cloud penetration. The CCP-CIP has imaged graupel in this case. The presence of these type of ice particles within convective clouds is very com-
370 mon in thunderstorms, and previous studies highlight the large frequency of lightning occurrence during the dry-to-wet season over the deforestation arc region of the Amazon (Albrecht et al., 2011; Williams et al., 2002). These results also highlight the role of aerosols from biomass burning on warm rain inhibition and on the aerosol invigoration effect due to the generation of large ice particles and lightning (Rosenfeld et al., 2008).

375 Regarding the values of r_e as a function of D_c , Figure 7a shows the estimated r_{ea} (calculated from the adiabatic CWC shown at Figure 7b) and measured r_e . The figure shows that the estimated values for r_{ea} are close to the r_e measurements for convective cloud passes at different D_c . Even though no raindrops were observed in the convective cloud, the figure shows similar values of r_{ea} and measured r_e (with r_{ea} slightly larger) as a function of D_c .

380 5.2.2 Results of analysis of r_e and D_c in clean and polluted regions

- Clean region

Figure 8a shows the measured N_d of a convective cluster over the Atlantic Ocean off the Brazilian coast (flight AC19). This region was classified as clean because N_d is about 300 cm⁻³ (see Table 3). The cloud base was located at 600 m above sea level at a temperature of 22 °C. Given the clean conditions over the ocean, the high relative humidity at sur-
385 face level and the low concentration of CCN lead to the formation of large droplets already close to cloud base. Figure 8b shows the estimated r_{ea} and the measured r_e as a function of D_c . Several cloud passes showed large droplets with $r_e \sim 13 \mu\text{m}$ at only 1660 m above cloud base. Figures 9a-b show the DSDs and CCP-CIP images for the cloud passes at the height where rain starts to form and at the greatest height measured above cloud base, respectively. Figure 9a shows that rain is initiated ($\text{DWC} > 0.01 \text{ g m}^{-3}$) already when the droplets become larger than about $r_e > 12 \mu\text{m}$. This is probably
390 due to the presence of GCCN over this maritime region.

Figure 10 shows the mean aerosol particle size distribution (PSD), as measured by the PCASP, just below cloud base for clean, polluted, and very polluted regions. The mean total number concentration of aerosol particles with sizes larger than 0.1 μm is about 1000 cm⁻³ over the Atlantic Ocean, whilst for polluted (very polluted) case this value is about three (ten) times larger. In addition, the mean total number concentration of particles measured by the CCP-CDP show con-
395 centration ten times greater for particles larger than 10 μm over the ocean in comparison with inland Amazon region. This figure indicates the presence of large aerosols particles with sizes greater than 1 μm (possibly GCCN) over the ocean. When it nucleates droplets, this type of aerosol accelerates the growth of droplets during the warm phase leading to a faster formation of raindrops than predicted by the adiabatic parcel model. About 3500 m above cloud base, large raindrops are observed in the CCP-CIP images (see Figure 9b). The low CWC indicates that most of it was already
400 converted into raindrops. These results highlight that under clean conditions, raindrops were formed mainly by warm

phase processes of cloud development. Even if the convective clouds reach colder temperatures, the low remaining amount of cloud water reduced a key ingredient for cloud electrification.

405 Before raindrops start to form ($D_c \sim 1,660$ m) updrafts were observed with most values $< 4 \text{ m s}^{-1}$, and when rain starts downdrafts starts to be evident (see Figure 3g at supplementary material). The values of vertical velocities measured at flight AC19 (clean region) were smaller than measured for flight AC07 (very polluted region). However, for both cases updrafts are more evident during droplets growth via condensation and downdrafts are stronger when precipitation particles are observed in the cloud. Strong updrafts ($\sim 10 \text{ m s}^{-1}$) are observed in polluted cases after ice starts to form (see Figure 3a at supplementary material), probably due to the latent heat release during freezing processes. An alternative explanation of updraft enhancement due to environmental conditions in these cases cannot be excluded.

410

-Polluted regions

The flights AC09 and AC18 were classified as polluted (see Table 3). These flights were performed over the northern Amazon region (see Figure 1a). Figure 11a shows the measured N_d from flight AC09. The cloud base was located about 1200 m above sea level at a temperature of 19.5 °C. Figure 11b shows the estimated r_{ea} and the measured r_e as a function of D_c . Values of $r_e > 13 \text{ }\mu\text{m}$ were observed for temperatures around 0 °C, indicating the possibility of rain starting at this height. Figure 12a-b shows the DSDs and CCP-CIP images from flight AC09 at the height where rain starts to form ($D_r \sim 3000$ m) and at the greatest height with measurements above cloud base. The CIP image at Figure 12b shows the first pass in which ice hydrometeors are observed mixed with supercooled rain drops. For lower levels only raindrops were observed. For flight AC18 cloud base was located about 1700 m above sea level at a temperature of 17 °C, and rain started to form in convective clouds when $D_r \sim 3800$ m. The measured N_d and the estimated r_{ea} and measured r_e as a function of D_c from flight AC18 are shown at Figures 4a-b at supplementary material. Figure 5a at the supplementary material shows that first rain drops in AC18 are observed at the -5.7 °C isotherm, and that they still remain liquid, or at least spherical, at the -11.4 °C isotherm (see Figure 5b at the supplementary material). Larger raindrops and a high amount of DWC were observed on AC09 for warmer temperatures than on flight AC18 (not shown). These results show that differences in cloud particle formation are associated with the D_c at which convective clouds start to form raindrops or ice, defined earlier as D_r and D_i . Flight AC18 has a droplet concentration, N_d , of up to 100 cm^{-3} greater than the measurements during AC09 (see Figure 4a at supplementary material). With higher N_d at cloud base, droplet growth via condensation in convective clouds is a less pronounced function of height due to the water vapor competition between droplets. Under these conditions, the collision and coalescence process and freezing of droplets are initiated at higher D_c (Freud and Rosenfeld, 2012; Rosenfeld et al., 2008). For this the reason, the formation of raindrops and ice particles on flight AC09 starts at lower D_c than on flight AC18 (assuming non-significant additional CCN activation above cloud base).

-Very polluted regions

435 Five flights were classified as very polluted (see Table 3): AC07, AC08, AC12, AC13, and AC20. The microphysical analysis of the measurements collected in growing convective cumulus during flight AC07 was already presented in Section 5.2.1. Figure 13a show the measured N_d from flight AC13, which was made in the same region as flight AC07. The figure shows that the values of N_d near cloud base on flight AC13 reach 2000 cm^{-3} , similar to AC07. However, the rate of decrease of N_d with height above cloud base is much smaller in AC13 compared to AC07. During flight AC13 the measurements of large updrafts (which increase supersaturation and induce new droplets activation) and large aerosol concentration above cloud base suggest the occurrence of additional CCN activation leading to the observed relative increase of N_d with height. This is supported by the fact that the observed r_e are smaller than the calculated r_{ea} , as shown

440

in Figure 13b. Only values below 13 μm are observed (maximum of 12 μm), indicating the suppression of raindrop formation. Indeed, no raindrops were observed in the CCP-CIP images from growing convective cumulus passes on this flight, and only cloud droplets and ice particles were detected. Figure 14 shows the DSD and CCP-CIP images at the start of glaciation ($D_i \sim 4800$ m). These results highlight the role of aerosols in inhibition of raindrop formation due to inducing a larger N_d and respective lower r_e , which leads to suppression of collision and coalescence processes in very polluted regions.

The measured N_d during flights AC08, AC12, and AC20 was greater above cloud base than at cloud base on several cloud passes (especially in flights AC08 and AC20; see Figures 6 and 7 in the supplementary material for these flights). In these flights the estimated r_{ea} values were larger than the measured r_e as a function of D_c and strong updrafts (up to 15 m s^{-1}) were observed above cloud base (see Figures 3b,d and h in the supplementary material). The acceleration of updrafts above the height of cloud base increase supersaturation and thus can induce additional CCN activation. For flights which we observed the increase of N_d with height, high aerosol concentration was observed indicating additional CCN activation above cloud base. During these flights, cloud profiling was performed up to $D_c \sim 3500$ m, and the values of measured r_e were smaller than 13 μm , indicating the suppression of raindrop formation. The analysis of the data from the cloud probe DSDs and CCP-CIP images indicates that indeed no raindrops were present on these flights (not shown). The measurements from AC07 and AC13 over very polluted regions in the Amazon suggest that no raindrops are formed in growing convective clouds under these conditions. Instead, large precipitation particles are formed at cold temperatures in the form of ice. The D_c at which these ice particles are formed depends on the size of the cloud droplets (r_e) at colder temperatures (larger droplets freeze earlier or at lower D_c) [Pruppacher et al., 1998]. This was previously documented by satellite retrievals (Rosenfeld et al., 2011), where glaciation temperatures of convective clouds were strongly dependent on r_e at the -5 $^\circ\text{C}$ isotherm, where smaller r_e were correlated with lower glaciation temperatures.

6. Discussion

The results from cloud probe measurements under clean, polluted, and very polluted conditions highlight the role of aerosol particles in rain and ice formation for growing convective cumulus. Figure 15 summarizes the estimated depths above cloud base at which initiation of rain and ice formation is observed (D_r and D_i), as well as the estimated D_c for rain initiation as indicated from r_{ea} by D_{I3} . This figure shows a close relationship between N_a and D_r of $D_r = (5 \pm 1.06) \cdot N_a$, demonstrating the capability to predict the minimum height at which raindrops are expected to form based on cloud base drop concentrations. For flights in which rain was observed (AC19, AC18, and AC09), D_r occurs at heights slightly greater than D_{I3} . For cases where neither rain nor ice were observed (AC08, AC12, and AC20), the estimated D_{I3} was not reached during the HALO cloud profiling flights. In addition, D_{I3} and D_i show similar values for flight AC07, whereas for flight AC13 the values are less comparable (probably due to an overestimation of N_a , and thus D_{I3} , caused by additional CCN activation above cloud base).

The linear relationship between N_a and D_{I3} indicates a regression slope of about $5 \text{ m (cm}^{-3}\text{)}^{-1}$ between D_{I3} and the calculated N_a for the Amazon during the dry-to-wet season. This value is slightly larger than the values observed by Freud and Rosenfeld (2012) for other locations around the globe (e.g., India and Israel). These clear linear relationships found between N_a and D_r ($\sim D_{I3}$) for different regions highlight the efficiency of the adiabatic parcel model to estimate the height of rain initiation within convective clouds in this study. Additional cloud processes associated such as GCCN, cloud and mixing with ambient air and other processes, which are not accounted for in this study, would produce deviations that are likely to be the cause of the observed scatter in the results.

485 For the flight in cleanest conditions (AC19), the presence of larger aerosol particles (possibly GCCN from sea spray) below cloud base leads to a faster growth of cloud droplets via condensation with height, and consequently r_e is smaller than 13 μm (see Figure 9a) for warm rain initiation. A similar decrease of r_e for rain initiation over ocean was observed by Konwar et al. (2012). While D_r is explained by N_d and well correlated with it, there is no correlation between N_d and D_i .

490 Figure 16 illustrates the vertical development of precipitation water content by symbols representing the amount of DWC and MPWC as a function of D_c and CDP-measured r_e . Also shown are the lines of r_{ea} as a function of D_c . The figure shows that raindrops began to form at r_e of 13 μm for AC09 and AC18. The r_e for rain initiation is slightly smaller (12 μm) on AC19; probably due to the sea spray giant CCN, which accelerate the coalescence for a given r_e . Mixed phase precipitation was initiated on flights AC07 and AC13, well below the height of D_{I3} at an r_e of 11.5 and 10.2 μm , respectively. Ice starts to form at lower temperatures when the cloud droplets are smaller, as manifested by D_i of -9 and -14 $^\circ\text{C}$ for flights AC07 and AC13, respectively. The remaining flights did not reach the height for rain initiation (AC08, 495 AC12, and AC20).

It is evident that raindrops form faster via collision and coalescence process in a cleaner atmosphere. For the polluted cases, raindrops form at colder temperatures (~ 0 $^\circ\text{C}$ and colder) via collision and coalescence than for clean conditions. Rain can initiate at supercooled temperatures, e.g., -5 $^\circ\text{C}$ on AC18. The raindrops were documented to start freezing at -9 $^\circ\text{C}$ in AC09. In very polluted conditions, only cloud droplets, but no raindrops were observed at $D_c < 4000$ m. In these 500 cases, precipitation was initiated as ice particles at $D_c > 4000$ m. These flights with completely suppressed warm rain were performed over the smoky deforestation arc. Measurements of large updrafts which increase supersaturation within cloud and the higher N_d above cloud base indicate new activation of cloud droplets for flight AC13 (not observed at AC07) in the course of the development of convective cumulus. This additional CCN activation leads to smaller r_e . For flights where additional CCN activation was significant, the differences between the estimated r_{ea} and the r_e measurements at same height are larger, because the adiabatic estimation does not consider the additional CCN activation of 505 droplets above cloud base and thus overestimates the observed size.

Figure 17 summarizes the findings from the vertical profiling flights. It illustrates the vertical microstructure of growing cumulus above the Amazon and the adjacent ocean in varying aerosol conditions. The figure highlights the differences of aerosol concentrations and cloud particles distribution within convective clouds over the Amazon basin (including 510 the Atlantic Ocean, forested and deforested regions). The aerosol concentration is smaller over the Atlantic Ocean and increase significantly at continental Amazon, especially over the deforestation arc due to biomass burning emissions from forest fires. As polluted is the atmosphere, larger is the number of droplets nucleated at cloud base and less efficient is the growth of cloud droplets via condensation with D_c . The new activation of CCN above cloud base also has shown to decrease the efficiency of cloud droplets growth due to the higher competition for water vapor available. The increase of aerosol concentration over the Amazon basin according to our findings has shown to suppress the warm rain 515 formation because larger cloud depths were necessary to raindrop starts to form (when cloud droplets have $r_e \sim 13\text{-}14$ μm). The additional aerosol concentrations observed at polluted regions from forest fires suppress rain such that most of hydrometeors are ice when they are at a size that allows distinguish their phase (~ 0.25 mm). In addition, the formation of ice particles was also delayed (or occurred at higher D_c) in more polluted atmosphere, because smaller cloud droplets freeze at lower temperatures. 520

7. Conclusions

This study focused on the effects of aerosol particle number concentration on the initiation of rain drops and ice hydrometeors in growing convective cumulus over the Amazon. Data from aerosol and cloud probes on board of the

525 HALO aircraft were used in the analysis. The values of the estimated N_a at cloud base were applied to classify the atmospheric conditions where convective clouds developed as a function of aerosol particle number concentration (i.e., clean, polluted, and very polluted regions). From the estimated N_a , the evolution of r_{ea} , the theoretical r_e assuming adiabatic growth of droplets, with cloud depth above cloud base (D_c) were compared with the observed r_e at the various heights. A DWC value of 0.01 g m^{-3} was used as a threshold for rain initiation or glaciation within clouds. Images from
530 the CCP-CIP probe were used to detect the presence of raindrops and/or ice hydrometeors. The results shown in previous sections support the following conclusions:

1. The use of $r_e \sim 13\text{-}14 \text{ }\mu\text{m}$ as a threshold for rain initiation is suitable for convective clouds formed at the Amazon basin during the dry season. It is in agreement with r_e of rain initiation elsewhere.
2. The evolution of the directly observed r_e follows generally that of the calculated r_{ea} due to the nearly
535 inhomogeneous mixing behavior of the convective clouds with the ambient air. Convective clouds are usually non-adiabatic systems because of strong wind/turbulence effects, heating and other factors, but the similarities of r_e and r_{ea} provided the capability to estimate D_r over the Amazon and others regions around the globe (e.g. India and Israel).
3. Rain initiation occurred higher in more polluted clouds, as manifested by higher D_c . Rain was initiated at
540 supercooled levels in moderately polluted clouds. In very polluted conditions, warm rain was suppressed completely. This was exacerbated by the occurrence of additional CCN activation above cloud base, which further reduced r_e compared to r_{ea} .
4. The initiation of ice hydrometeors is also delayed to greater D_c in more polluted clouds, because smaller drops freeze at colder temperatures due to suppressed ice multiplication processes (Hallett and Mossop, 1974). Ice was initiated mostly by freezing raindrops in cases when warm rain formation was not completely suppressed.
5. Both the D_{I3} and D_r increased linearly with N_a , in agreement with the theoretical considerations of Freud and Rosenfeld (2012). Despite the suspected occasional additional CCN activation, r_e was sufficiently close to r_{ea}
545 to allow a linear relationship in the form of $D_r = (5 \pm 1.06) \cdot N_a$. The deviation from exact linear relationship can be associated to additional cloud processes such as GCCN, cloud and mixing with ambient air etc. The magnitude of these additional processes is insufficient to mask the linear relationship. The observations suggest also that, in the absence of new droplet activation above cloud base, D_{I3} is very similar to D_i under
550 very polluted conditions, where raindrops are not formed at warmer temperatures.

These results show that even moderate amounts of smoke, which fill most of the Amazon basin during the drier season,
555 are sufficient to suppress warm rain and elevate its initiation to above the $0 \text{ }^\circ\text{C}$ isotherm level. This results in a suppression of rain from small clouds and an invigoration in the deep clouds, as hypothesized by Rosenfeld et al. (2008). While the net effect on rainfall amount is unknown, the redistribution of rain intensities and the resulting vertical latent heating profiles are likely to affect the regional hydrological cycle in ways that need to be studied further.

560 Acknowledgements

The first two authors of this study were supported by project BACCHUS European Commission FP7-603445. The generous support of the ACRIDICON-CHUVA campaign by the Max Planck Society, the German Aerospace Center (DLR), FAPESP (São Paulo Research Foundation), and the German Science Foundation (Deutsche Forschungsgemeinschaft, DFG) within the DFG Priority Program (SPP 1294) “Atmospheric and Earth System Research with the Research
565 Aircraft HALO (High Altitude and Long Range Research Aircraft)” is greatly appreciated. This study was also supported by EU Project HAIC under FP7-AAT-2012-3.5.1-1. C. Mahnke and R. Weigel received funding by the German Fed-

eral Ministry of Education and Research (BMBF, Bundesministerium für Bildung und Forschung) within the joint RO-MIC-project SPITFIRE (01LG1205A). In addition, the German Science Foundation within DFG SPP 1294 HALO by contract no VO1504/4-1 and contract no JU 3059/1-1 contribute to support this study. The first author also acknowl-
570 edges the financial support from the Brazilian funding agencies CAPES and CNPq during his Ph.D. studies.

References

- 575 Albrecht, R. I., Morales, C. A. and Silva Dias, M. A. F.: Electrification of precipitating systems over the Amazon: Physical processes of thunderstorm development, *J. Geophys. Res.*, 116(D8), D08209, doi:10.1029/2010JD014756, 2011.
- Andreae, M. O.: Correlation between cloud condensation nuclei concentration and aerosol optical thickness in remote
580 and polluted regions, *Atmos. Chem. Phys.*, 9(2), 543–556, doi:10.5194/acp-9-543-2009, 2009.
- Andreae, M. O., Rosenfeld, D., Artaxo, P., Costa, A. A., Frank, G. P., Longo, K. M. and Silva-Dias, M. A. F.: Smoking rain clouds over the Amazon., *Science*, 303(5662), 1337–42, doi:10.1126/science.1092779, 2004.
- 585 Andreae, M. O., Artaxo, P., Beck, V., Bela, M., Freitas, S., Gerbig, C., Longo, K., Munger, J. W., Wiedemann, K. T. and Wofsy, S. C.: Carbon monoxide and related trace gases and aerosols over the Amazon Basin during the wet and dry seasons, *Atmos. Chem. Phys.*, 12(13), 6041–6065, doi:10.5194/acp-12-6041-2012, 2012.
- Artaxo, P., Martins, J. V., Yamasoe, M. A., Procópio, A. S., Pauliquevis, T. M., Andreae, M. O., Guyon, P., Gatti, L. V.
590 and Leal, A. M. C.: Physical and chemical properties of aerosols in the wet and dry seasons in Rondônia, Amazonia, *J. Geophys. Res. D Atmos.*, 107(20), 1–14, doi:10.1029/2001JD000666, 2002.
- Artaxo, P., Rizzo, L. V., Brito, J. F., Barbosa, H. M. J., Arana, A., Sena, E. T., Cirino, G. G., Bastos, W., Martin, S. T. and
595 Andreae, M. O.: Atmospheric aerosols in Amazonia and land use change: from natural biogenic to biomass burning conditions, *Faraday Discuss.*, 165, 203–235, doi:10.1039/C3FD00052D, 2013.
- Baumgardner, D., Brenguier, J. L., Bucholtz, A., Coe, H., DeMott, P., Garrett, T. J., Korolev, A., Krämer, M., Petzold, A., Strapp, W., Pilewskie, P., Taylor, J., Twohy, C., Wendisch, M., Bachalo, W., and Chuang, P. Airborne instruments to measure atmospheric aerosol particles, clouds and radiation: A cook's tour of mature and emerging technology. *At-
600 mospheric Research*, 102(1), 10-29, 2011.
- Beals, M. J., Fugal, J. P., Shaw, R. A., Lu, J., Spuler, S. M. and Stith, J. L.: Holographic measurements of inhomogeneous cloud mixing at the centimeter scale, , 350(6256), 87–90, doi:10.1126/science.aab0751, 2015.
- 605 Braga, R. C., Rosenfeld, D., Weigel, R., Jurkat, T., Andreae, M. O., Wendisch, M., Pöhlker, M. L., Klimach, T., Pöschl, U., Pöhlker, C., Voigt, C., Mahnke, C., Borrmann, S., Albrecht, R. I., Molleker, S., Vila, D. A., Machado, L. A. T., and Artaxo, P.: Comparing parameterized versus measured microphysical properties of tropical convective cloud bases during the ACRIDICON–CHUVA campaign, *Atmos. Chem. Phys.*, 17, 7365–7386, <https://doi.org/10.5194/acp-17-7365-2017>, 2017.

610

Brenguier, J. L., Bachalo, W. D., Chuang, P. Y., Esposito, B. M., Fugal, J., Garrett, T., Gayet, J. F., Gerber, H., Heymsfield, A., Kokhanovsky, A., Korolev, A., Lawson, R. P., Rogers, D. C., Shaw, R. A., Strapp, W. and Wendisch, M.: In Situ Measurements of Cloud and Precipitation Particles, in *Airborne Measurements for Environmental Research: Methods and Instruments*, pp. 225–301., 2013.

615

Burnet, F. and Brenguier, J.L.: Observational Study of the Entrainment-Mixing Process in Warm Convective Clouds, *J. Atmos. Sci.*, 64(6), 1995–2011, doi:10.1175/JAS3928.1, 2007.

620

Chen, R., R. Wood, Z. Li, R. Ferraro, and F. Chang: Studying the vertical variation of cloud droplet effective radius using ship and spaceborne remote sensing data, *J. Geophys. Res.*, 113, D00A02, doi:10.1029/2007JD009596, 2008.

625

Fan, J., Leung, L. R., Demott, P. J., Comstock, J. M., Singh, B., Rosenfeld, D., Tomlinson, J. M., White, A., Prather, K. A., Minnis, P., Ayers, J. K. and Min, Q.: Aerosol impacts on California winter clouds and precipitation during calwater 2011: Local pollution versus long-range transported dust, *Atmos. Chem. Phys.*, 14(1), 81–101, doi:10.5194/acp-14-81-2014f, 2014.

Freud, E. and Rosenfeld, D.: Linear relation between convective cloud drop number concentration and depth for rain initiation, *J. Geophys. Res. Atmos.*, 117(2), 1–13, doi:10.1029/2011JD016457, 2012.

630

Freud, E., Rosenfeld, D. and Kulkarni, J. R.: Resolving both entrainment-mixing and number of activated CCN in deep convective clouds, *Atmos. Chem. Phys.*, 11(24), 12887–12900, doi:10.5194/acp-11-12887-2011, 2011.

635

Frey, W., Borrmann, S., Kunkel, D., Weigel, R., De Reus, M., Schlager, H., Roiger, A., Voigt, C., Hoor, P., Curtius, J., Krämer, M., Schiller, C., Volk, C. M., Homan, C. D., Fierli, F., Di Donfrancesco, G., Ulanovsky, A., Ravegnani, F., Sitnikov, N. M., Viciani, S., D'Amato, F., Shur, G. N., Belyaev, G. V., Law, K. S. and Cairo, F.: In situ measurements of tropical cloud properties in the West African Monsoon: Upper tropospheric ice clouds, mesoscale convective system outflow, and subvisual cirrus, *Atmos. Chem. Phys.*, 11(12), 5569–5590, doi:10.5194/acp-11-5569-2011, 2011.

640

Gerber, H.: Microphysics of marine stratocumulus clouds with two drizzle modes, *J. Atmos. Sci.*, 53(12), 1649–1662, 1996.

Hallett, J.; Mossop, S. C. C. Production of secondary ice particles during the riming process. *Nature*, v. 249, n. 5452, p. 26–28, 1974.

645

Khain, A., Rosenfeld, D. and Pokrovsky, A.: Aerosol impact on the dynamics and microphysics of deep convective clouds, *Q. J. R. Meteorol. Soc.*, 131, 2639–2663 ST – Aerosol impact on the dynamics and, doi:10.1256/qj.04.62, 2005.

650

Khain, A., Ovtchinnikov, M., Pinsky, M., Pokrovsky, A. and Krugliak, H.: Notes on the state-of-the-art numerical modeling of cloud microphysics, *Atmos. Res.*, 55(3-4), 159–224, doi:10.1016/S0169-8095(00)00064-8, 2000.

Klein, S. A., McCoy, R. B., Morrison, H., Ackerman, A. S., Avramov, A., Boer, G. De, Chen, M., Cole, J. N. S., Del

- Genio, A. D., Falk, M., Foster, M. J., Fridlind, A., Golaz, J.C., Hashino, T., Harrington, J. Y., Hoose, C., Khairoutdinov, Konwar, M., Maheskumar, R. S., Kulkarni, J. R., Freud, E., Goswami, B. N. and Rosenfeld, D.: Aerosol control on depth of warm rain in convective clouds, *J. Geophys. Res. Atmos.*, 117(13), 1–10, doi:10.1029/2012JD017585, 2012, 655
- Kuhn, U., Ganzeveld, L., Thielmann, A., Dindorf, T., Schebeske, G., Welling, M., Sciare, J., Roberts, G., Meixner, F. X., Kesselmeier, J., Lelieveld, J., Kolle, O., Ciccioli, P., Lloyd, J., Trentmann, J., Artaxo, P. and Andreae, M. O.: Impact of Manaus City on the Amazon Green Ocean atmosphere: ozone production, precursor sensitivity and aerosol load, *Atmos. Chem. Phys.*, 10(19), 9251–9282, doi:10.5194/acp-10-9251-2010, 2010, 660
- Lance, S.: Coincidence errors in a cloud droplet probe (CDP) and a cloud and aerosol spectrometer (CAS), and the improved performance of a modified CDP, *J. Atmos. Ocean. Technol.*, 29(10), 1532–1541, doi:10.1175/JTECH-D-11-00208.1, 2012, 665
- Lance, S., Brock, C. A., Rogers, D. and Gordon, J. A.: Water droplet calibration of the Cloud Droplet Probe (CDP) and in-flight performance in liquid, ice and mixed-phase clouds during ARCPAC, *Atmos. Meas. Tech.*, 3(6), 1683–1706, doi:10.5194/amt-3-1683-2010, 2010, 670
- M. F., Larson, V. E., Liu, X., Luo, Y., McFarquhar, G. M., Menon, S., Neggers, R. A. J., Park, S., Poellot, M. R., Schmidt, J. M., Sednev, I., Shipway, B. J., Shupe, M. D., Spangenberg, D. A., Sud, Y. C., Turner, D. D., Veron, D. E., Salzen, K. Von, Walker, G. K., Wang, Z., Wolf, A. B., Xie, S., Xu, K.-M., Yang, F. and Zhang, G.: Intercomparison of model simulations of mixed-phase clouds observed during the ARM Mixed-Phase Arctic Cloud Experiment. I: single-layer cloud, *Q. J. R. Meteorol. Soc.*, 135(641), 979–1002, doi:10.1002/qj.416, 2009, 675
- Lee, G. W., Seed, A. W. and Zawadzki, I.: Modeling the variability of drop size distributions in space and time, *J. Appl. Meteorol. Climatol.*, 46(6), 742–756, doi:10.1175/JAM2505.1, 2007.
- Li, Z., Li, C., Chen, H., Tsay, S. C., Holben, B., Huang, J., Li, B., Maring, H., Qian, Y., Shi, G., Xia, X., Yin, Y., Zheng, Y. and Zhuang, G.: East Asian Studies of Tropospheric Aerosols and their Impact on Regional Climate (EAST-AIRC): An overview, *J. Geophys. Res. Atmos.*, 116(4), doi:10.1029/2010JD015257, 2011, 680
- Liu, P. S. K., Leaitch, W. R., Strapp, J. W., and Wasey, M. A., Response of Particle Measuring Systems airborne ASASP and PCASP to NaCl and latex particles: *Aerosol Sci. Tech.*, 16, 83-95, 1992, 685
- Machado L, Silva Dias M, Morales C, Fisch G, Vila D, Albrecht R, Goodman S, Calheiros A, Biscaro T, Kummerow C, Cohen J, Fitzjarrald D, Nascimento E, Sakamoto M, Cunningham C, Chaboureaud J, Petersen W, Adams D, Baldini L, Angelis C, Sapucci L, Salio P, Barbosa H, Landulfo E, Souza R, Blakeslee R, Bailey J, Freitas S, Lima W, Tokay A , The Chuva Project: How Does Convection Vary across Brazil?, *Bull. Am. Meteorol. Soc.*, doi: 10.1175/BAMS-D-13-00084.1, 2014, 690
- Mallaun, C., Giez, A. and Baumann, R.: Calibration of 3-D wind measurements on a single-engine research aircraft,

- Atmos. Meas. Tech., 8(8), 3177–3196, doi:10.5194/amt-8-3177-2015, 2015.
- 695
- Martin, S. T., Artaxo, P., Machado, L. A. T., Manzi, A. O., Souza, R. A. F., Schumacher, C., Wang, J., Andreae, M. O., Barbosa, H. M. J., Fan, J., Fisch, G., Goldstein, A. H., Guenther, A., Jimenez, J. L., Pöschl, U., Silva Dias, M. A., Smith, J. N. and Wendisch, M.: Introduction: Observations and Modeling of the Green Ocean Amazon (GoAmazon2014/5), Atmos. Chem. Phys., 16(8), 4785–4797, doi:10.5194/acp-16-4785-2016, 2016.
- 700
- Paluch, I. R. (1979). The entrainment mechanism in Colorado cumuli. *J. Atmos. Sci.*, 36:2467–2478
- Pinsky, M. B. and Khain, A.: Effects of in-cloud nucleation and turbulence on droplet spectrum formation in cumulus clouds, *Q. J. R. Meteorol. Soc.*, 128(580), 501–533, doi:10.1256/003590002321042072, 2002.
- 705
- Pöhlker, M. L., Pöhlker, C., Klimach, T., Angelis, I. H. de, Barbosa, H. M. J., Brito, J., Samara Carbone, Cheng, Y., Chi, X., Ditas, F., Ditz, R., Gunthe, S. S., Kesselmeier, J., Könemann, T., Lavrič, J. V., Martin, S. T., Moran-Zuloaga, D., Rose, D., Saturno, J., Su, H., Thalman, R., Walter, D., Wang, J., Wolff, S., Artaxo, P., Andreae, M. O. and Pöschl, U.: Long-term observations of atmospheric aerosol, cloud condensation nuclei concentration and hygroscopicity in the Amazon rain forest – Part 1 : Size-resolved characterization and new model parameterizations for CCN prediction, Atmos. Chem. Phys., (July), doi:10.5194/acp-2016-519, 2016.
- 710
- Pöschl, U., Martin, S. T., Sinha, B., Chen, Q., Gunthe, S. S., Huffman, J. A., Borrmann, S., Farmer, D. K., Garland, R. M., Helas, G., Jimenez, J. L., King, S. M., Manzi, A., Mikhailov, E., Pauliquevis, P., Petters, M. D., Prenni, A. J., Roldin, P., Rose, D., Schneider, J., Su, H., Zorn, S. R., Artaxo, P. and Andreae, M. O.: Rainforest Aerosols as Biogenic Nuclei of Clouds and Precipitation in the Amazon, *Science* (80-.), 329(2010), 1513–1516, doi:10.1126/science.1191056, 2010.
- 715
- Prabha, T. V., A. Khain, R. S. Maheshkumar, G. Pandithurai, J. R. Kulkarni, M. Konwar, and B. N. Goswami: Microphysics of premonsoon and monsoon clouds as seen from in situ measurements during the Cloud Aerosol Interaction and Precipitation Enhancement Experiment (CAIPEEX), *J. Atmos. Sci.*, 68, 1882–1901, 2011.
- 720
- Pruppacher, H. R., Klett, J. D. and Wang, P. K.: Microphysics of Clouds and Precipitation, *Aerosol Sci. Technol.*, 28, 381–382, doi:10.1080/02786829808965531, 1998.
- 725
- Ramanathan, V., Crutzen, P. J., Lelieveld, J., Mitra, A. P., Althausen, D., Anderson, J., Andreae, M. O., Cantrell, W., Cass, G. R., Chung, C. E., Clarke, A. D., Coakley, J. A., Collins, W. D., Conant, W. C., Dulac, F., Heintzenberg, J., Heymsfield, A. J., Holben, B., Howell, S., Hudson, J., Jayaraman, A., Kiehl, J. T., Krishnamurti, T. N., Lubin, D., McFarquhar, G., Novakov, T., Ogren, J. A., Podgorny, I. A., Prather, K., Priestley, K., Prospero, J. M., Quinn, P. K., Rajeev, K., Rasch, P., Rupert, S., Sadourny, R., Satheesh, S. K., Shaw, G. E., Sheridan, P. and Valero, F. P. J.: Indian Ocean Experiment: An integrated analysis of the climate forcing and effects of the great Indo-Asian haze, *J. Geophys. Res.*, 106(D22), 28371, doi:10.1029/2001JD900133, 2001.
- 730
- Rosenfeld, D.: Suppression of Rain and Snow by Urban and Industrial Air Pollution, *Science* (80-.), 287, 1793–1796, doi:10.1126/science.287.5459.1793, 2000.
- 735

- Rosenfeld, D. and Gutman, G.: Retrieving microphysical properties near the tops of potential rain clouds by multispectral analysis of AVHRR data, *Atmos. Res.*, 34(1-4), 259–283, doi:10.1016/0169-8095(94)90096-5, 1994.
- 740 Rosenfeld, D. and Lensky, I. M.: Satellite-Based Insights into Precipitation Formation Processes in Continental and Maritime Convective Clouds, *Bull. Am. Meteorol. Soc.*, 79(11), 2457–2476, doi:10.1175/1520-0477, 1998.
- Rosenfeld, D. and Woodley, W. L. W.: Deep convective clouds with sustained supercooled liquid water down to -37.5 degrees C, *Nature*, 405(6785), 440–2, 2000.
- 745 Rosenfeld, D., Lohmann, U., Raga, G. B., O’Dowd, C. D., Kulmala, M., Fuzzi, S., Reissell, A. and Andreae, M. O.: Flood or drought: how do aerosols affect precipitation?, *Science*, 321(5894), 1309–13, doi:10.1126/science.1160606, 2008.
- 750 Rosenfeld, D., Yu, X., Liu, G., Xu, X., Zhu, Y., Yue, Z., Dai, J., Dong, Z., Dong, Y. and Peng, Y.: Glaciation temperatures of convective clouds ingesting desert dust, air pollution and smoke from forest fires, *Geophys. Res. Lett.*, 38(21), 2006–2010, doi:10.1029/2011GL049423, 2011.
- Rosenfeld, D., Wang, H. and Rasch, P. J.: The roles of cloud drop effective radius and LWP in determining rain properties in marine stratocumulus, *Geophys. Res. Lett.*, 39(13), 1–6, doi:10.1029/2012GL052028, 2012a.
- 755 Rosenfeld, D., Williams, E., Andreae, M. O., Freud, E., Pöschl, U. and Rennó, N. O.: The scientific basis for a satellite mission to retrieve CCN concentrations and their impacts on convective clouds, *Atmos. Meas. Tech.*, 5(8), 2039–2055, doi:10.5194/amt-5-2039-2012, 2012b.
- 760 Rosenfeld, D., Andreae, M. O., Asmi, A., Chin, M., De Leeuw, G., Donovan, D. P., Kahn, R., Kinne, S., Kiveks, N., Kulmala, M., Lau, W., Schmidt, K. S., Suni, T., Wagner, T., Wild, M. and Quaas, J.: Global observations of aerosol-cloud-precipitation-climate interactions, *Rev. Geophys.*, 52(4), 750–808, doi:10.1002/2013RG000441, 2014a.
- 765 Rosenfeld, D., Fischman, B., Zheng, Y., Goren, T. and Giguzin, D.: Combined satellite and radar retrievals of drop concentration and CCN at convective cloud base, *Geophys. Res. Lett.*, 41(9), 3259–3265, doi:10.1002/2014GL059453, 2014b.
- Rosenfeld, D., Liu, G., Yu, X., Zhu, Y., Dai, J., Xu, X. and Yue, Z.: High-resolution (375 m) cloud microstructure as seen from the NPP/VIIRS satellite imager, *Atmos. Chem. Phys.*, 14(5), 2479–2496, doi:10.5194/acp-14-2479-2014, 2014c.
- 770 Segal, Y., Pinsky, M. and Khain, A.: The role of competition effect in the raindrop formation, *Atmos. Res.*, 83(1), 106–118, doi:10.1016/j.atmosres.2006.03.007, 2007.
- 775 Tao, W., Chen, J. and Li, Z.: Impact of aerosols on convective clouds and precipitation, *Rev. Geophys.*, 50, RG2001, doi:10.1029/2011RG000369, 2012.
- Twomey, S.: The nuclei of natural cloud formation part II: The supersaturation in natural clouds and the variation of

cloud droplet concentration, *Geofis. Pura e Appl.*, 43(1), 243–249, doi:10.1007/BF01993560, 1959.

780

VanZanten, M., B. Stevens, G. Vali, and D. Lenschow: Observations of drizzle in nocturnal marine stratocumulus, *J. Atmos. Sci.*, 62(1), 88–106, 2005

785

Voigt, C., Schumann, U., Jurkat, T., Schäuble, D., Schlager, H., Petzold, A., Gayet, J. F., Krämer, M., Schneider, J., Borrmann, S., Schmale, J., Jessberger, P., Hamburger, T., Lichtenstern, M., Scheibe, M., Gourbeyre, C., Meyer, J., Kübbeler, M., Frey, W., Kalesse, H., Butler, T., Lawrence, M. G., Holzäpfel, F., Arnold, F., Wendisch, M., Döpelheuer, A., Gottschaldt, K., Baumann, R., Zöger, M., Sölch, I., Rautenhaus, M. and Dörnbrack, A.: In-situ observations of young contrails—overview and selected results from the CONCERT campaign. *Atmospheric Chemistry and Physics*, 10(18), 9039-9056, 2010.

790

Voigt, C., Schumann, U., Jessberger, P., Jurkat, T., Petzold, A., Gayet, J. F., Krmer, M., Thornberry, T. and Fahey, D. W.: Extinction and optical depth of contrails, *Geophys. Res. Lett.*, 38(11), doi:10.1029/2011GL047189, 2011.

795

Voigt, C., Schumann, U., Minikin, A., Abdelmonem, A., Afchine, A., Borrmann, S., Boettcher, M., Buchholz, B., Bugliaro, L., Costa, A., Curtius, J., Dollner, M., Dörnbrack, A., Dreiling, V., Ebert, V., Ehrlich, A., Fix, A., Forster, L., Frank, F., Fütterer, D., Giez, A., Graf, K., Groß, J., Groß, S., Heimerl, K., Heinold, B., Hüneke, T., Järvinen, E., Jurkat, T., Kaufmann, S., Kenntner, M., Klingebiel, M., Klimach, T., Kohl, R., Krämer, M., Krisna, T., Luebke, A., Mayer, B., Mertes, S., Molleker, S., Petzold, A., Pfeilsticker, K., Port, M., Rapp, M., Reutter, P., Rolf, C., Rose, D., Sauer, D., Schäfler, A., Schlage, R., Schnaiter, M., Schneider, J., Spelten, N., Spichtinger, P., Stock, P., Walser, A., Weigel, R., Weinzierl, B., Wendisch, M., Werner, F., Wernli, H., Wirth, M., Zahn, A., Ziereis, H. and Zöger, M.: ML-CIRRUS - The airborne experiment on natural cirrus and contrail cirrus with the high-altitude long-range research aircraft HALO, *Bull. Am. Meteorol. Soc.*, doi:10.1175/BAMS-D-15-00213.1, 2017.

800

805

Wendisch, M., Pöschl, U., Andreae, M. O., Machado, L. A. T., Albrecht, R., Schlager, H., Rosenfeld, D., Martin, S. T., Abdelmonem, A., Afchine, A., Araùjo, A., Artaxo, P., Aufmhoff, H., Barbosa, H. M. J., Borrmann, S., Braga, R., Buchholz, B., Cecchini, M. A., Costa, A., Curtius, J., Dollner, M., Dorf, M., Dreiling, V., Ebert, V., Ehrlich, A., Ewald, F., Fisch, G., Fix, A., Frank, F., Fütterer, D., Heckl, C., Heidelberg, F., Hüneke, T., Jäkel, E., Järvinen, E., Jurkat, T., Kanter, S., Kästner, U., Kenntner, M., Kesselmeier, J., Klimach, T., Knecht, M., Kohl, R., Kölling, T., Krämer, M., Krüger, M., Krisna, T. C., Lavric, J. V., Longo, K., Mahnke, C., Manzi, A. O., Mayer, B., Mertes, S., Minikin, A., Molleker, S., Münch, S., Nillius, B., Pfeilsticker, K., Pöhlker, C., Roiger, A., Rose, D., Rosenow, D., Sauer, D., Schnaiter, M., Schneider, J., Schulz, C., de Souza, R. A. F., Spanu, A., Stock, P., Vila, D., Voigt, C., Walser, A., Walter, D., Weigel, R., Weinzierl, B., Werner, F., Yamasoe, M. A., Ziereis, H., Zinner, T. and Zöger, M.: The ACRIDICON-CHUVA campaign: Studying tropical deep convective clouds and precipitation over Amazonia using the new German research aircraft HALO, *Bull. Am. Meteorol. Soc.*, 160128144638003, doi:10.1175/BAMS-D-14-00255.1, 2016.

810

815

Williams, E.: Contrasting convective regimes over the Amazon: Implications for cloud electrification, *J. Geophys. Res.*, 107(D20), 1–19, doi:10.1029/2001JD000380, 2002.

820

Appendix – A

Cloud properties uncertainties

825 The uncertainties calculations of cloud properties estimated from CCP-CDP probe were described in Braga et al. (2017). The uncertainties of r_e , r_v , r_{ea} , r_{va} are $\sim 10\%$, while for CWC and M_v the uncertainties are about 30%. The calculation of N_a uncertainty is described below.

N_a uncertainty

830 The uncertainty of N_a is calculated based on the uncertainty of slope between CWCa and M_{va} . The two maximum/minimum acceptable slope lines of N_a can be used to estimate the uncertainty of the N_a of the best fit line. The principle behind this is that if we were to take another complete set of data, we would find a new best fit slope. The maximum amount by which it is likely to differ from our existing best fit slope is about half the difference of the maximum and minimum acceptable slopes that we have. So this can be used as an uncertainty estimate:

$$835 \text{ Slope uncertainty} = \frac{[(\text{maximum slope}) - (\text{minimum slope})]}{2} \quad (\text{A.1})$$

The absolute values of N_a uncertainty is shown at Table 3. The relative uncertainty of N_a values in mean terms is $\sim 21\%$ for all flights analyzed.

840 **Figure captions**

Figure 1 a) HALO flight tracks during the ACRIDICON-CHUVA experiment. The flight number is indicated at the bottom by colors; b) Flight patterns below and in convective clouds during the ACRIDICON-CHUVA campaign.

845 Figure 2 a) Precipitation probability as a function of r_e for the CCP-CDP probe for different DWC thresholds (black – DWC > 0.01 g m⁻³; blue – DWC > 0.02 g m⁻³; green – DWC > 0.03 g m⁻³; gold – DWC > 0.05 g m⁻³; red – DWC > 0.1 g m⁻³). The dashed line indicates the number of cases (in seconds for each 1-s cloud pass) for each r_e size interval (right axis); b) Similar for the CAS-DPOL probe.

850 Figure 3 Cloud droplet concentration measured with CCP-CDP as a function of temperature for flight AC07. Each dot indicates a 1-Hz average concentration. The sample number (N) and the approximate start time of the cloud profile are shown at the top of the panel.

855 Figure 4 a) Mean cloud droplet size distribution calculated from the CCP-CDP data for a cloud pass at cloud base during flight AC07. The flight number, initial time of cloud pass, and duration in seconds are shown at the top of graph. The mean total number of droplets (N_{dmean}), the maximum total number of droplets (N_{dmax}) in one second for this cloud pass, and the approximate height (H) and temperature (T) are shown at the upper-right corner of the graph; b) Cloud droplet effective radius (r_e) calculated from CCP-CDP as a function of temperature indicated with dots. The black line indicates the estimated adiabatic effective radius (r_{ea}) as a function of temperature.

860 Figure 5a-c. Droplet size distribution composite from the CCP-CDP and CCP-CIP probes (left panel). Similar for indicated cloud water content (CWC) in the right panel. Indicated at the top of the panels are the HALO flight number, date, time of flight (UTC), duration of cloud pass in seconds, temperature (T) and altitude (H) above sea level, and the mean values for the total number of droplets (N_d), CWC, DWC, RWC, and r_e . The color bars indicate the height of HALO during the cloud pass. On the right side of the panels CCP-CIP images corresponding to the cloud pass are shown.

865

Figure 6 Image taken from the HALO cockpit just before the aircraft penetration of a convective cloud with lightning activity during flight AC07. In this case, the cloud pass height was 9,022 m (temperature ~ -25 °C) and the maximum CWC measured was 0.55 g m⁻³.

870 Figure 7 a) Cloud droplet effective radius (r_e) as a function of cloud depth (D_c) for flight AC07. The line indicates the r_e estimated for adiabatic growth (r_{ea}) from cloud base (dashed lines indicate the r_{ea} values considering the uncertainty of the estimate). The height of 0 °C is indicated by a black horizontal bar across the r_{ea} line. The estimated adiabatic number of droplets (N_a) at cloud base is shown at the top of the figure. b) Similar to a) for Cloud water content (adiabatic values are shown by lines).

875

Figure 8 a) Cloud droplet concentrations measured with the CCP-CDP as a function of temperature for flight AC19. Each dot indicates 1Hz average concentration. The sample number in seconds (N) and the start time of the cloud profile are shown at the top of the panel; b) Similar to Figure 7 for flight AC19.

880 Figures 9 a-b) Similar to Figures 5a-c for flight AC19.

885 Figure 10 Cumulative aerosol size distribution below cloud base calculated from the PCASP probe for typical clean, polluted, and very polluted regions (solid line) for flights AC12 (very polluted), AC18 (polluted), and AC19 (clean). Similar for cumulative cloud droplet size distribution calculated with CCP-CDP (dashed line). The flight numbers are indicated by colors at the top of the panel.

890 Figure 11 a) Cloud droplet concentrations measured with the CCP-CDP as a function of temperature for flight AC09. Each dot indicates 1-Hz average concentration. The sample number in seconds (N) and the start time of the cloud profile are shown at the top of the panel; b) Similar to Figure 9 for flight AC09.

Figures 12 a-b) Similar to Figures 5a-c for flight AC09.

895 Figure 13 a) Cloud droplet concentration measured with the CCP-CDP probe as a function of temperature for flight AC13. Each dot indicates a 1-Hz average concentration. The sample number and the approximate time of the cloud profile are shown at the top of the panel; b) Similar to figure 7 for Flight AC13.

Figures 14 Similar to Figures 5a-c for flight AC13.

900 Figure 15 Cloud depth (D_c) as a function of the estimated adiabatic number of droplets (N_d) at cloud base. D_c for adiabatic cloud droplet effective radius (r_{ea}) equal 13 μm (or D_{13}) are indicated by triangles. Similar for cloud depth of rain initiation (D_r) [indicated by circles] and cloud depth for ice initiation (D_i) [indicated by asterisk]. The flight numbers are indicated by colors on the right side of the panel. The values of D_{13} , D_r , and D_i are shown in Table 1. The uncertainties of N_d estimates are shown by horizontal error bars. The vertical error bars indicate the cloud depth between D_r and D_{r-1} or D_i and D_{i-1} . The black line indicates the linear equation for D_{13} as a function of N_d for all flights, where: $D_r = (5 \pm 1.06)N_d$.

910 Figure 16 CDP-measured cloud droplet effective radius (r_e) (colored dots) and estimated cloud droplet adiabatic effective radius (r_{ea}) (colored lines) as a function of cloud depth (D_c) for all flights (indicated by colors). The height of 0 °C is indicated by a horizontal bar across the r_{ea} line. The circles indicate the approximate values of drizzle water content (DWC) calculated from the CCP-CIP data, the range of DWC values is indicated in the table at the upper-right side of the figure. The star symbols indicate approximate mixed phase drizzle water content (MPWC) values calculated from the CCP-CIP data (indicated in the table at the bottom-right side of the figure). The temperature in °C of rain or ice initiation (D_r and D_i , respectively) is indicated by colored numbers close to the circle or star symbols.

915 Figure 17. General characteristics of growing convective cumulus formed over the Amazon basin during the dry season. The heights of cloud base are higher over continental Amazon due to the smaller relative humidity in comparison with the maritime region. Convective clouds formed over the Atlantic Ocean, near the Brazilian coast, have smaller cloud droplets concentration (N_d) at cloud base due to the smaller concentration of aerosol and updraft speeds below cloud base. The initiation of warm rain (D_r) is observed at lower cloud depths (~ 2 km or $\sim 10^\circ\text{C}$) from collision and coalescence processes. When convective clouds are more continental, larger aerosol concentration and updrafts are observed below cloud base, leading to larger N_d nucleated at cloud base (as observed above forested and deforested

925 regions). Over the forest D_r is observed near 0°C, whilst for the deforestation arc region the collision and coalescence processes are totally suppressed and the formation of ice particles took place at higher altitudes in the clouds in very polluted conditions, because the resulting smaller cloud droplets froze at colder temperatures compared to the larger drops in the less polluted cases.

Table captions

Table 1. List of abbreviations and symbols.

930 Table 2. Description of cloud probes, size range intervals and hydrometeor shapes observed on CCP-CIP images used to calculate CWC, DWC, RWC and MPWC.

Table 3. Classification of each flight as a function of N_a at cloud base. The values of cloud base height (Cbh) and temperature (T), D_{I3} , D_r and D_i in m and temperatures in °C are also shown for convective cloud measurements of each flight. Additionally, information about the height of D_{r-1} , D_{i-1} , T_r , T_i , T_{i-1} , NLP and W_{max} is also shown for each flight. The uncertainties of N_a and D_{I3} estimates are described at Appendix A.

935

Tables

Table 1. List of abbreviations and symbols.

Abbreviation/notation	Description	Units
ACRIDICON-CHUVA	Aerosol, Cloud, Precipitation, and Radiation Interactions and Dynamics of Convective Cloud Systems - CHUVA (Cloud processes of the main precipitation systems in Brazil: A contribution to cloud resolving modeling and to the GPM [Global Precipitation Measurements])	-
CAS-DPOL	Cloud and Aerosol Spectrometer	-
C_{bh}	Cloud base height	m
CCP-CDP	Cloud Combination Probe - Cloud Droplet Probe	-
CCP-CIP	Cloud Combination Probe - Cloud Imaging Probe	-
CCN	Cloud Condensation Nuclei	cm^{-3}
CWC	Cloud water content	g m^{-3}
CWC_a	Adiabatic cloud water content	g m^{-3}
D_c	Cloud depth - distance from cloud base	m
D_r	Cloud depth where first drizzle with drop shape was detected	m
D_{r-1}	Nearest cloud depth below D_r without raindrop	m
D_i	Cloud depth where first drizzle with ice shape was detected	m
D_{i-1}	Nearest cloud depth below D_i without ice particles	m
DWC	Drizzle Water Content	g m^{-3}
DSD	Cloud-droplet size distribution	$\text{cm}^{-3} \mu\text{m}^{-1}$
D_{13}	Cloud depth where $r_{ea} = 13 \mu\text{m}$	m
IN	Ice Nuclei	cm^{-3}
K	The collection kernel of a pair of droplets	$\text{cm}^{-3} \text{s}^{-1}$
LWC	Liquid Water Content	g m^{-3}
MPWC	Mixed Phase Water Content	g m^{-3}
M_v	Mean volume cloud droplet	μm^{-3}
M_{va}	Adiabatic mean volume cloud droplet	μm^{-3}
N_a	Adiabatic number concentration of droplets	cm^{-3}
N_d	Number concentration of droplets	cm^{-3}
N_d^*	Effective number of droplets concentration at cloud base	cm^{-3}
NLS	Number of altitude levels sampled	-
PCASP	Passive Cavity Aerosol Spectrometer Probe	-
PSD	Aerosol particle size distribution	$\text{cm}^{-3} \mu\text{m}^{-1}$
r_e	The effective radius of the cloud droplet spectra	μm
r_{ea}	The adiabatic effective radius of the cloud droplet spectra	μm
r_v	The mean volume radius of the cloud droplets	μm
RWC	Rainwater Content	g m^{-3}
S	Supersaturation	%
T	Temperature	$^{\circ}\text{C}$
T_r	Temperature of rain initiation	$^{\circ}\text{C}$
T_i	Temperature of ice initiation	$^{\circ}\text{C}$
T_{i-1}	Nearest temperature greater than T_i without ice particles	$^{\circ}\text{C}$
W	Vertical velocity	m s^{-1}
W_{max}	Maximum vertical velocity during the cloud profiling flight	m s^{-1}

940 Table 2. Description of cloud probes, size range intervals and hydrometeor shapes observed on CCP-CIP images used to calculate CWC, DWC, RWC and MPWC.

Abbreviation/Notation	Instrument	Size range	Hydrometeor shapes
CWC	CCP-CDP/CAS-DPOL	3-50 μm	Cloud droplets
DWC	CCP-CIP	75-250 μm	Cloud droplets and raindrops
RWC	CCP-CIP	250-960 μm	Cloud droplets and raindrops
MPWC	CCP-CIP	75-960 μm	Cloud droplets and ice particles

945

950

955

960

965

970

975

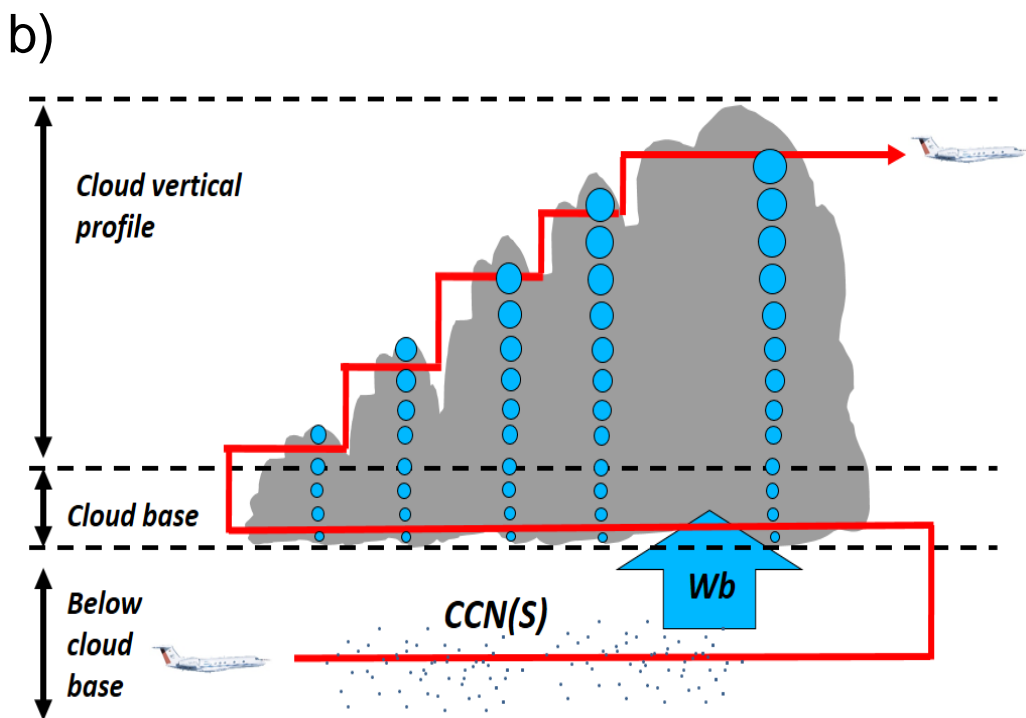
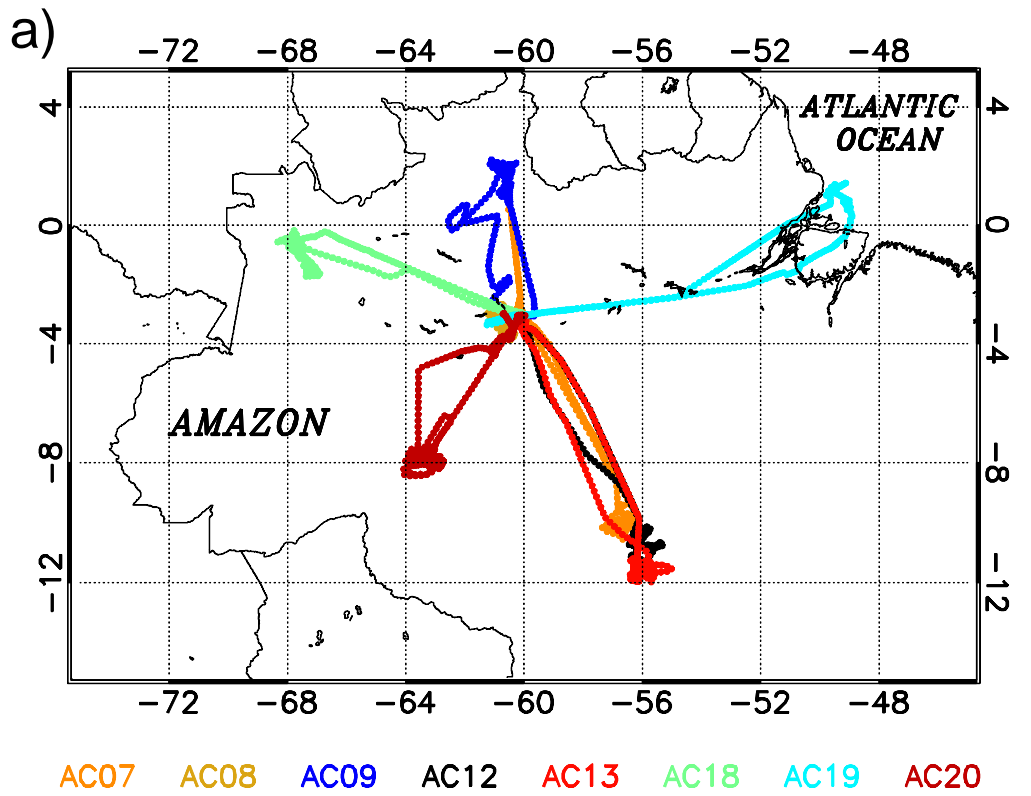
980

985

Table 3. Classification of each flight as a function of N_a at cloud base. The values of cloud base height (Cbh) and temperature (T), D_{I3} , D_r and D_i in m and temperatures in °C are also shown for convective cloud measurements of each flight. Additionally, information about the height of D_{r-l} , D_{i-l} , T_r , T_i , T_{i-l} , T_l , NLP and W_{max} is also shown for each flight. The uncertainties of N_a and D_{I3} estimates are described at Appendix A.

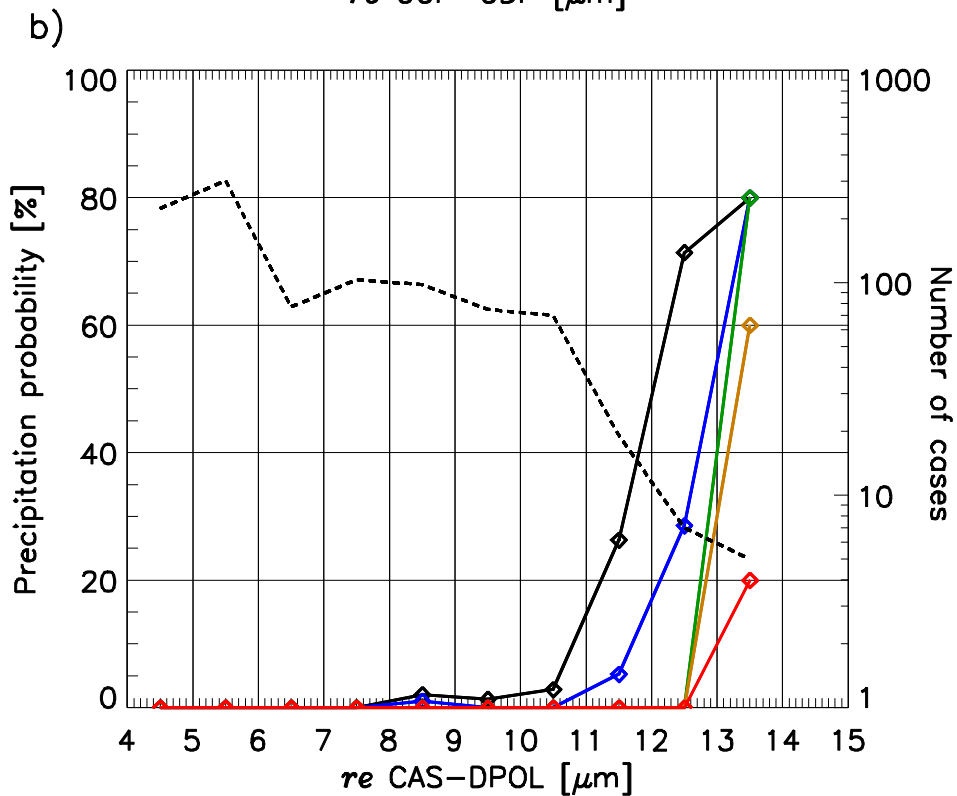
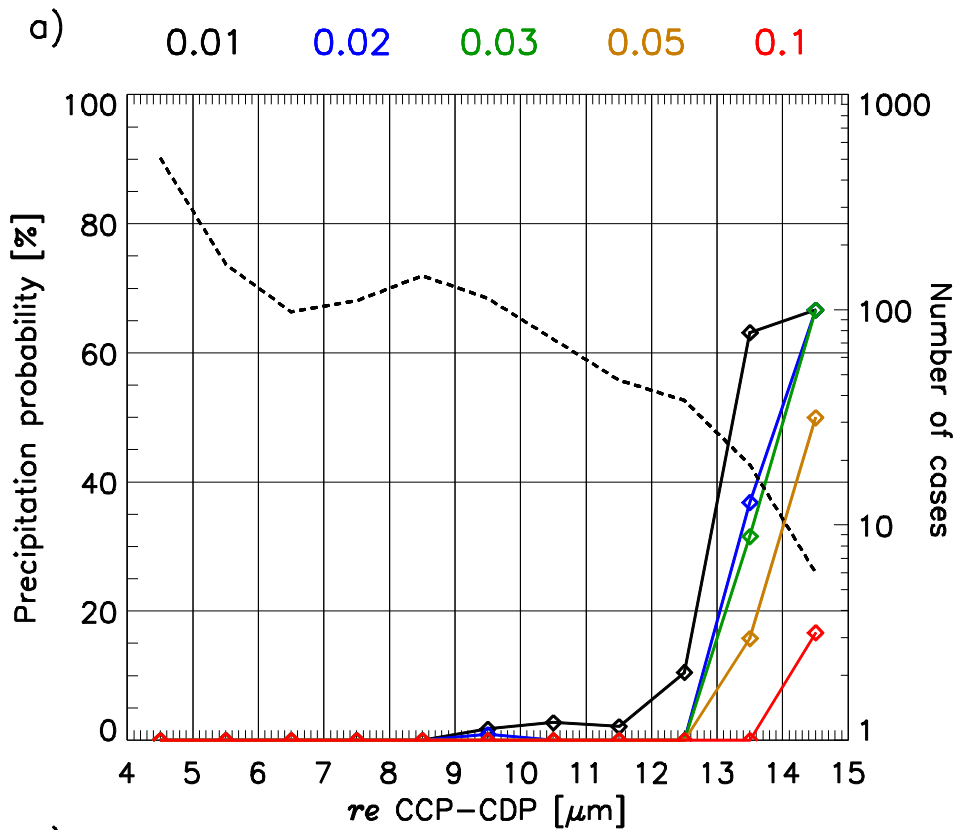
Flight	Cbh (m)/ T (°C)	N_a (cm ⁻³)	D_{I3} (m)	D_{r-l} (m)	D_r (m)	T_r (°C)	D_{i-l} (m)	T_{i-l} (°C)	D_i (m)	T_l (°C)	NLS	W_{max} (m s ⁻¹)	Classification
AC07	1900 / 15	963 ± 236	4500 ± 1104	-	-	-	3631	-5.3	4537	-9.1	14	13.09	very polluted
AC08	1100 / 20	920 ± 162	3900 ± 690	-	-	-	-	-	-	-	10	8.2	very polluted
AC09	1200 / 19.5	566 ± 98	2400 ± 420	2300	3000	2.4	4570	-6.0	5217	-9.2	15	8.8	polluted
AC12	2200 / 15.5	1546 ± 434	9000 ± 2540	-	-	-	-	-	-	-	12	18.9	very polluted
AC13	2200 / 15.5	1080 ± 234	5500 ± 1194	-	-	-	4240	-9.0	4800	-14.1	12	9.2	very polluted
AC18	1700 / 17	666 ± 114	2900 ± 512	3100	3800	-5.7	-	-	-	-	13	19.9	polluted
AC19	600 / 22	276 ± 54	1000 ± 198	1150	1660	10	-	-	-	-	13	8.49	clean
AC20	1900 / 16.5	987 ± 224	5000 ± 1130	-	-	-	-	-	-	-	8	16.6	very polluted

Figures

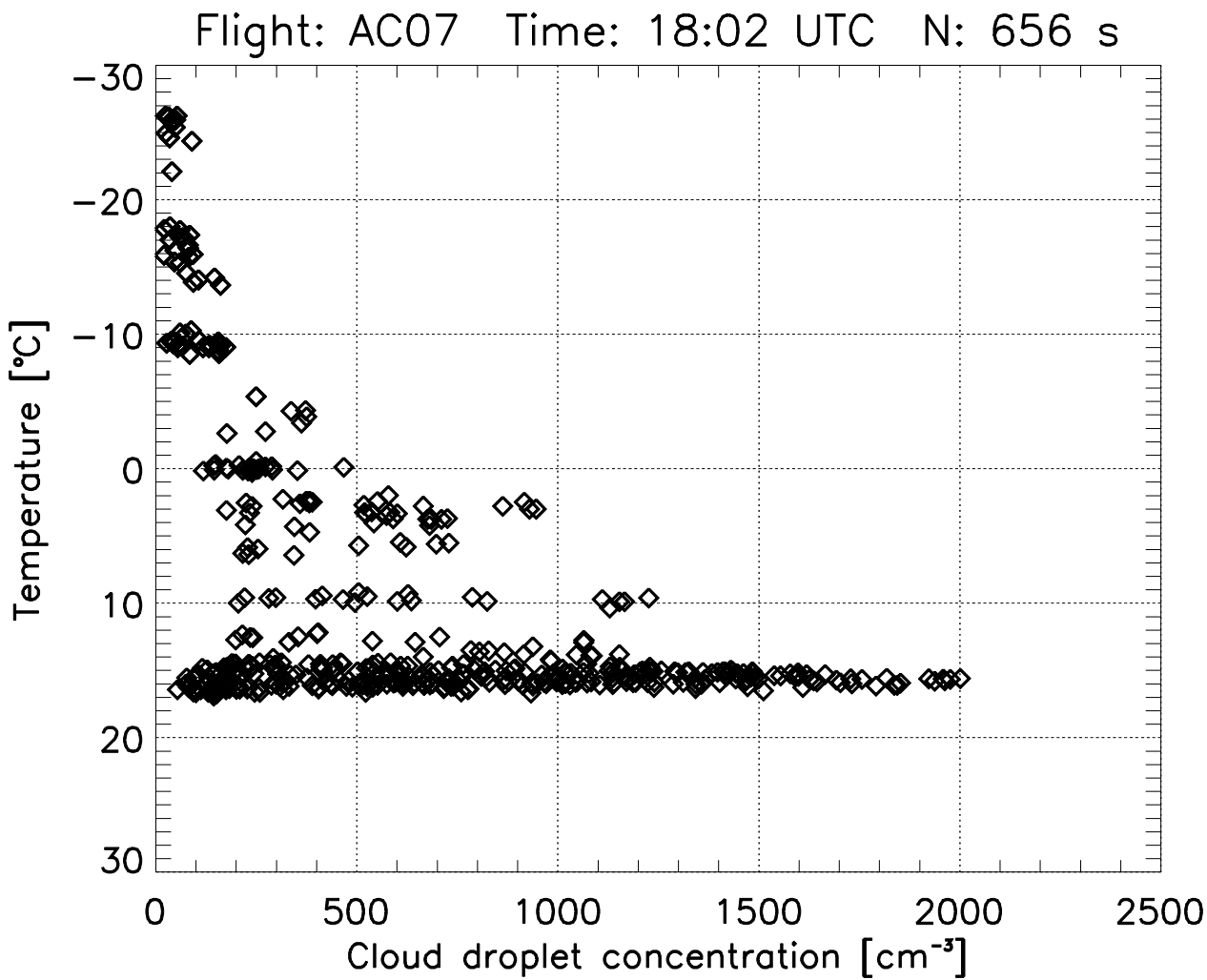


1010

Figure 1 a) HALO flight tracks during the ACRIDICON-CHUVA experiment. The flight number is indicated at the bottom by colors; b) Flight patterns below and in convective clouds during the ACRIDICON-CHUVA campaign.

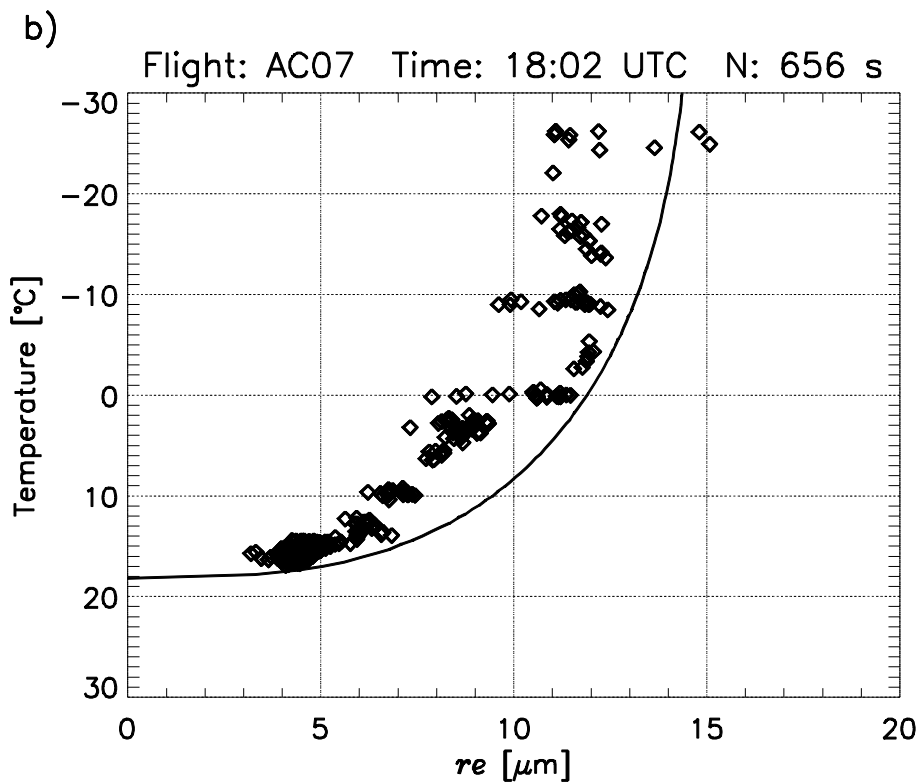
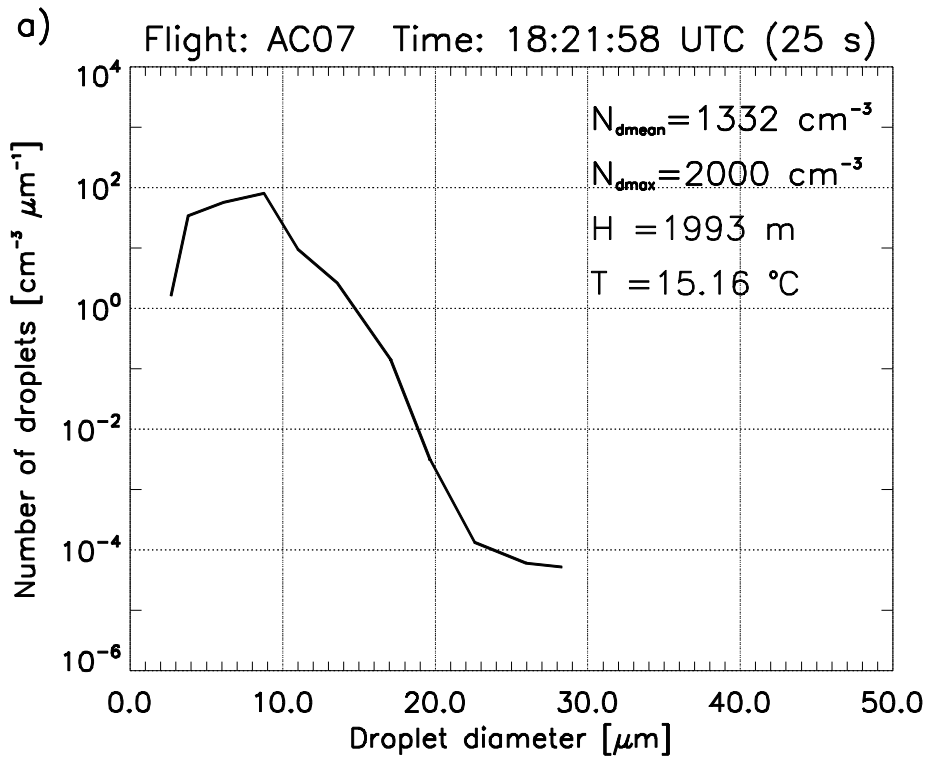


1015 Figure 2 a) Precipitation probability as a function of r_e for the CCP-CDP probe for different DWC thresholds (black – DWC > 0.01 g m⁻³; blue – DWC > 0.02 g m⁻³; green – DWC > 0.03 g m⁻³; gold – DWC > 0.05 g m⁻³; red – DWC > 0.1 g m⁻³). The dashed line indicates the number of cases (in seconds for each 1-s cloud pass) for each r_e size interval (right axis); b) Similar for the CAS-DPOL probe.



1020

Figure 3 Cloud droplet concentration measured with CCP-CDP as a function of temperature for flight AC07. Each dot indicates a 1-Hz average concentration. The sample number (N) and the approximate start time of the cloud profile are shown at the top of the panel.



1025

1030

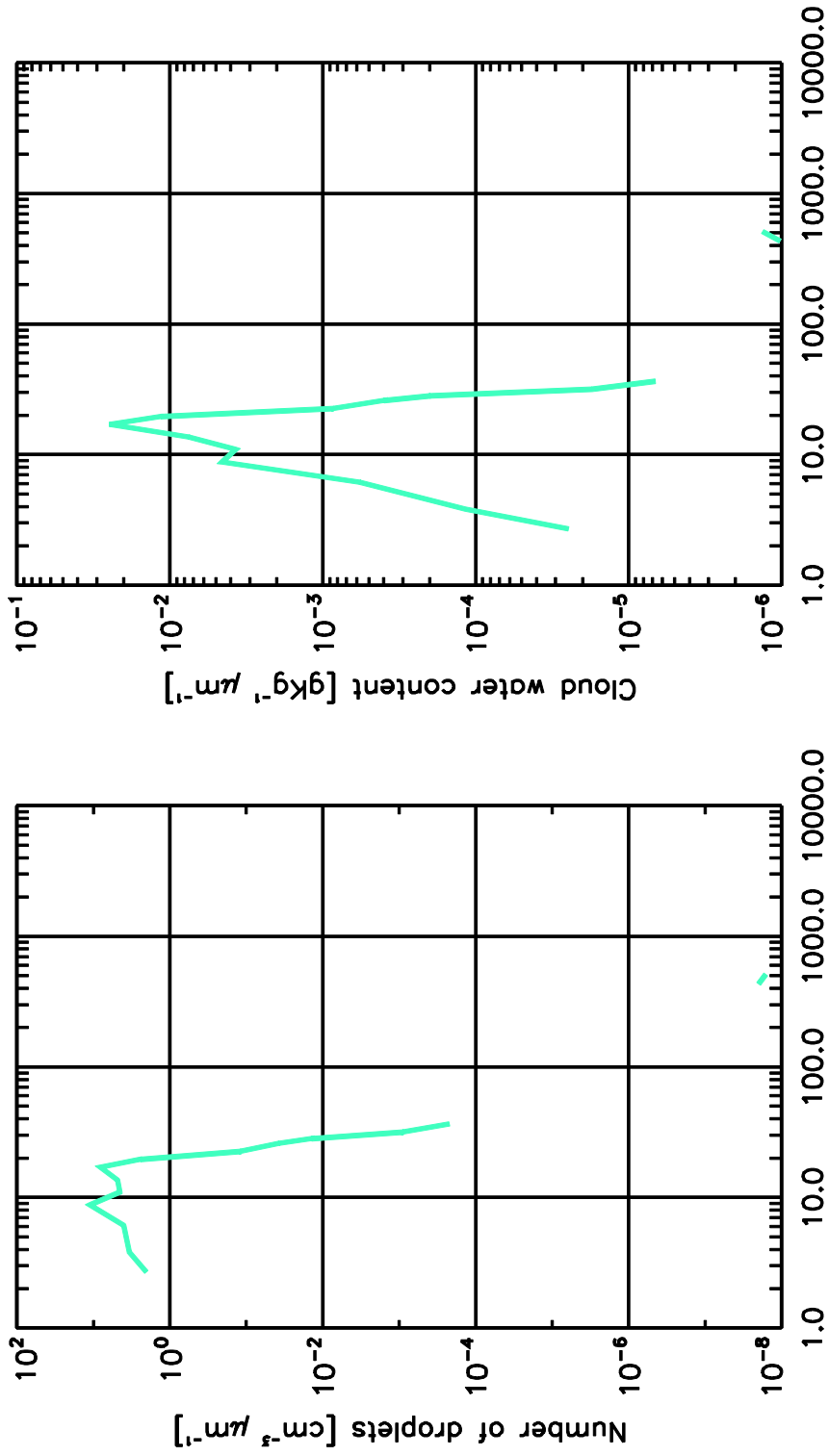
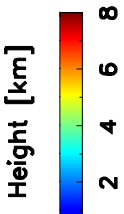
1035

Figure 4 a) Mean cloud droplet size distribution calculated from the CCP-CDP data for a cloud pass at cloud base during flight AC07. The flight number, initial time of cloud pass, and duration in seconds are shown at the top of graph. The mean total number of droplets ($N_{d\text{mean}}$), the maximum total number of droplets ($N_{d\text{max}}$) in one second for this cloud pass, and the approximate height (H) and temperature (T) are shown at the upper-right corner of the graph; b) Cloud droplet effective radius (r_e) calculated from CCP-CDP as a function of temperature indicated with dots. The black line indicates the estimated adiabatic effective radius (r_{ea}) as a function of temperature.

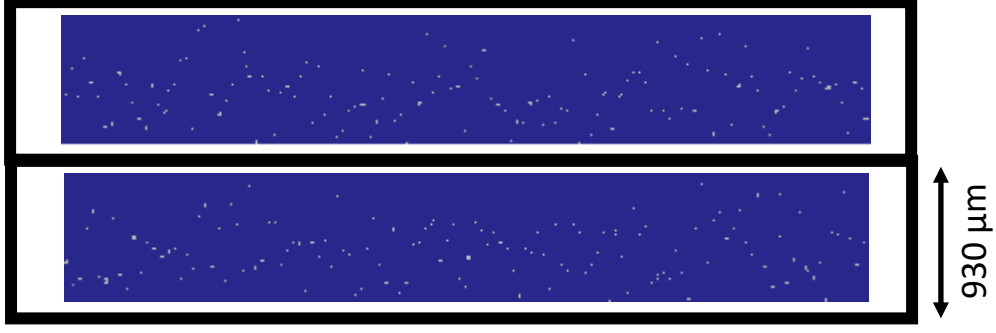
a)

Flight: AC07 Date: 2014/09/06 18:48 UTC [09 s]

H=3612 m $N_p=435 \text{ cm}^{-3}$ $DWC=0.00 \text{ gm}^{-3}$
 T=5.7 °C $CWC=0.730 \text{ gm}^{-3}$ $RWC=0.00 \text{ gm}^{-3}$



CCP-CIP Images



CCP-CIP + CCP-CIP droplet diameter [μm]

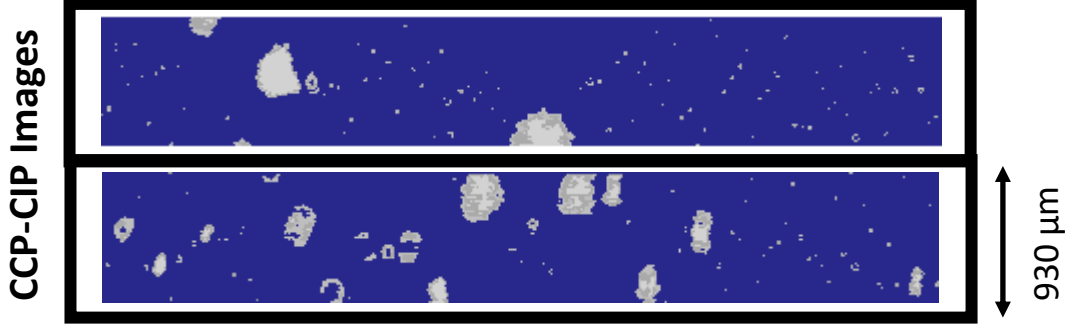
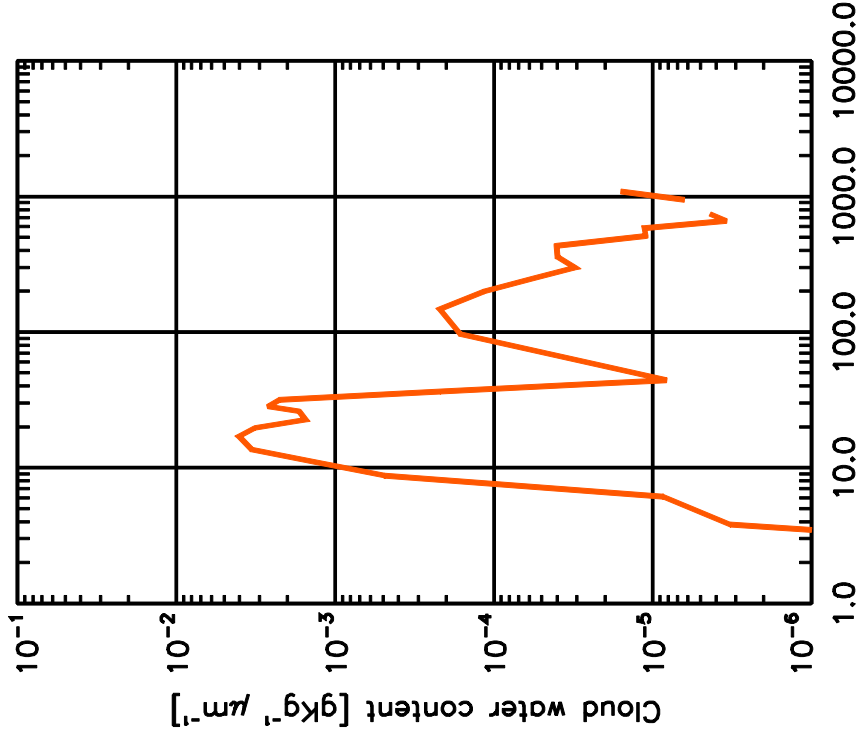
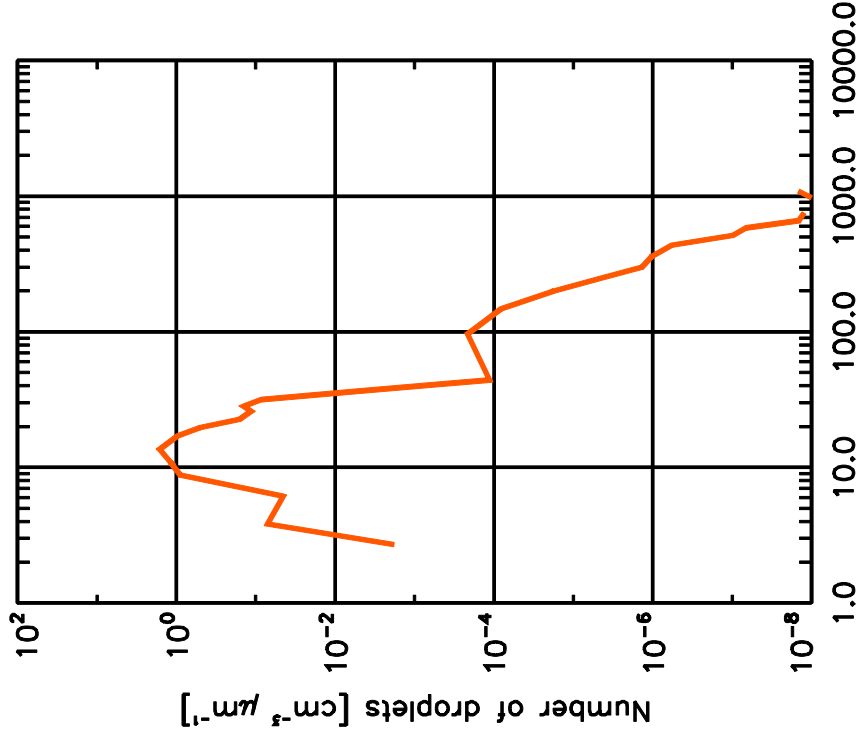
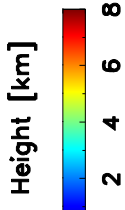
b)

Flight: AC07 Date: 2014/09/06 20:14 UTC [06 s]

H=6437 m
T=-9.1 °C
N_c=83 cm⁻³
CWC=0.270 gm⁻³

DWC=0.05 gm⁻³
RWC=0.05 gm⁻³

$r_e = 11.48 \mu\text{m}$



CCP-CDP + CCP-CIP droplet diameter [μm]

c)

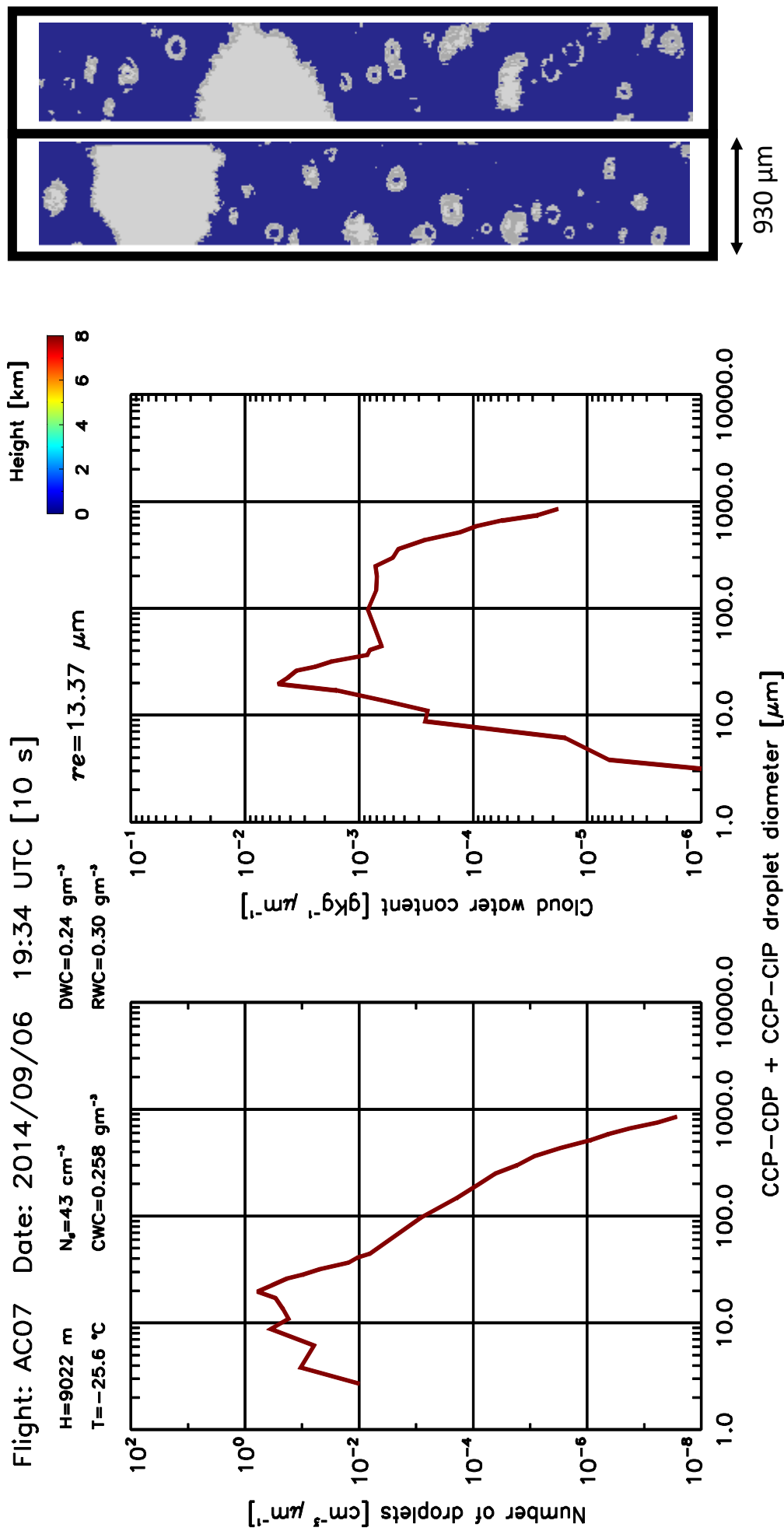


Figure 5a-c. Mean droplet size distribution composite from the CCP-CDP and CCP-CIP probes (left panel). Similar for indicated cloud water content in the right panel. Indicated at the top of the panels are the HALO flight number, date, time of flight (UTC), duration of cloud pass in seconds, temperature (T) and altitude (H) above sea level, and the mean values for the total number of droplets (N_d), CWC, DWC, RWC, and r_e . The color bars indicate the height of HALO during the cloud pass. On the right side of the panels CCP-CIP images corresponding to the cloud pass are shown.



Figure 6 Image taken from the HALO cockpit just before the aircraft penetration of a convective cloud with lightning activity during flight AC07. In this case, the cloud pass height was 9,022 m (temperature ~ -25 °C) and the maximum CWC measured was 0.55 g m⁻³.

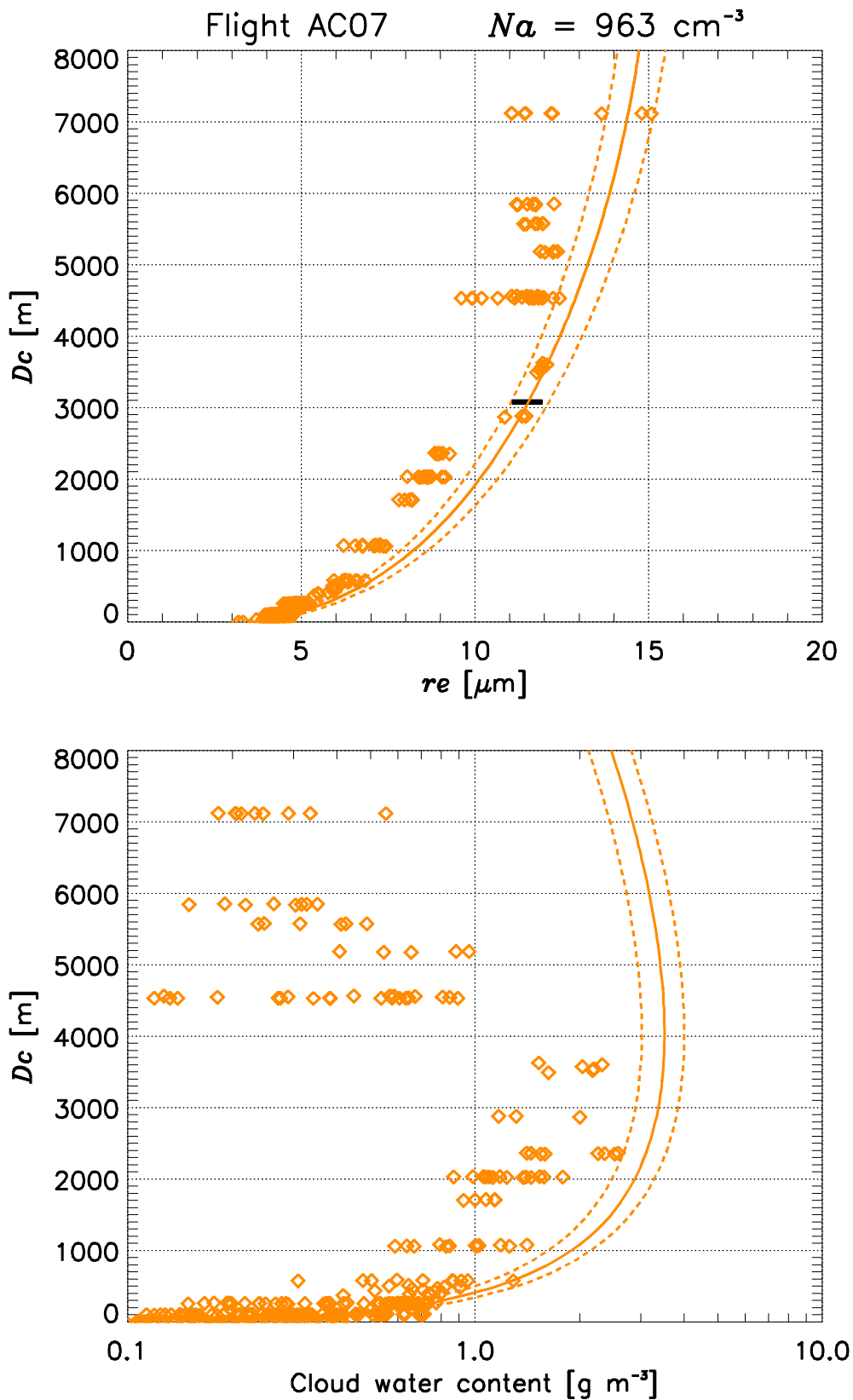


Figure 7 a) Cloud droplet effective radius (r_e) as a function of cloud depth (D_c) for flight AC07. The line indicates the r_e estimated for adiabatic growth (r_{ea}) from cloud base (dashed lines indicate the r_{ea} values considering the uncertainty of the estimate). The height of 0 °C is indicated by a black horizontal bar across the r_{ea} line. The estimated adiabatic number of droplets (N_a) at cloud base is shown at the top of the figure. b) Similar to a) for Cloud water content (adiabatic values are shown by lines).

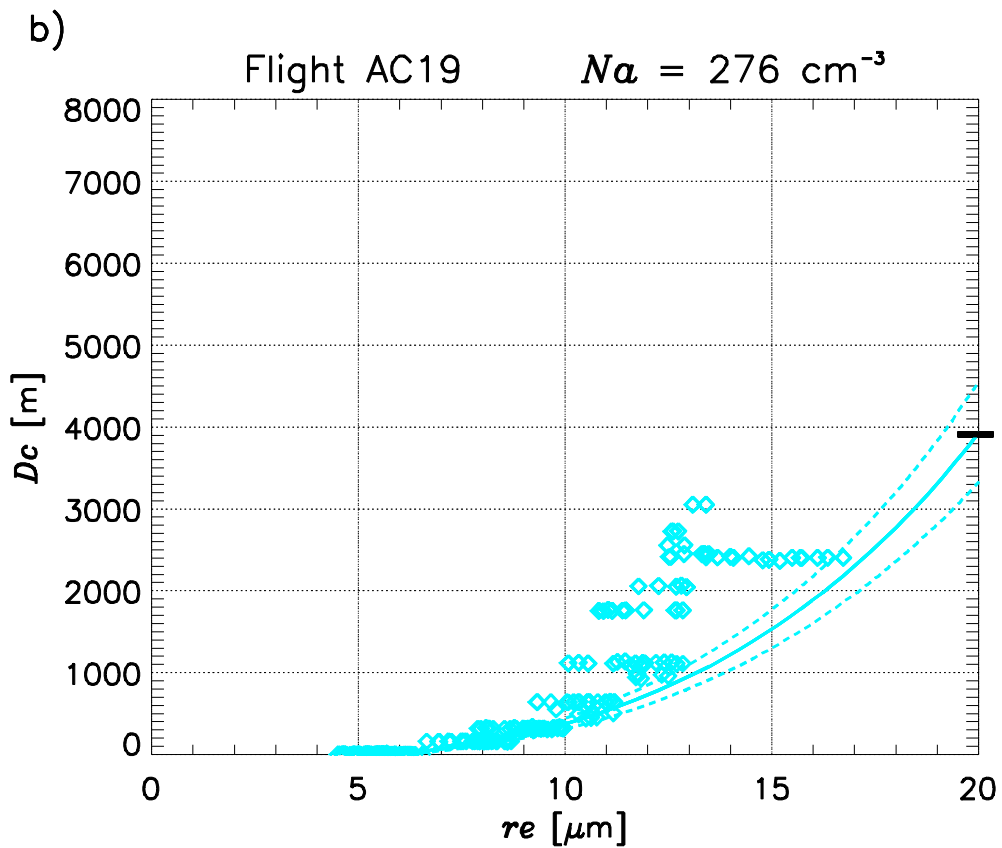
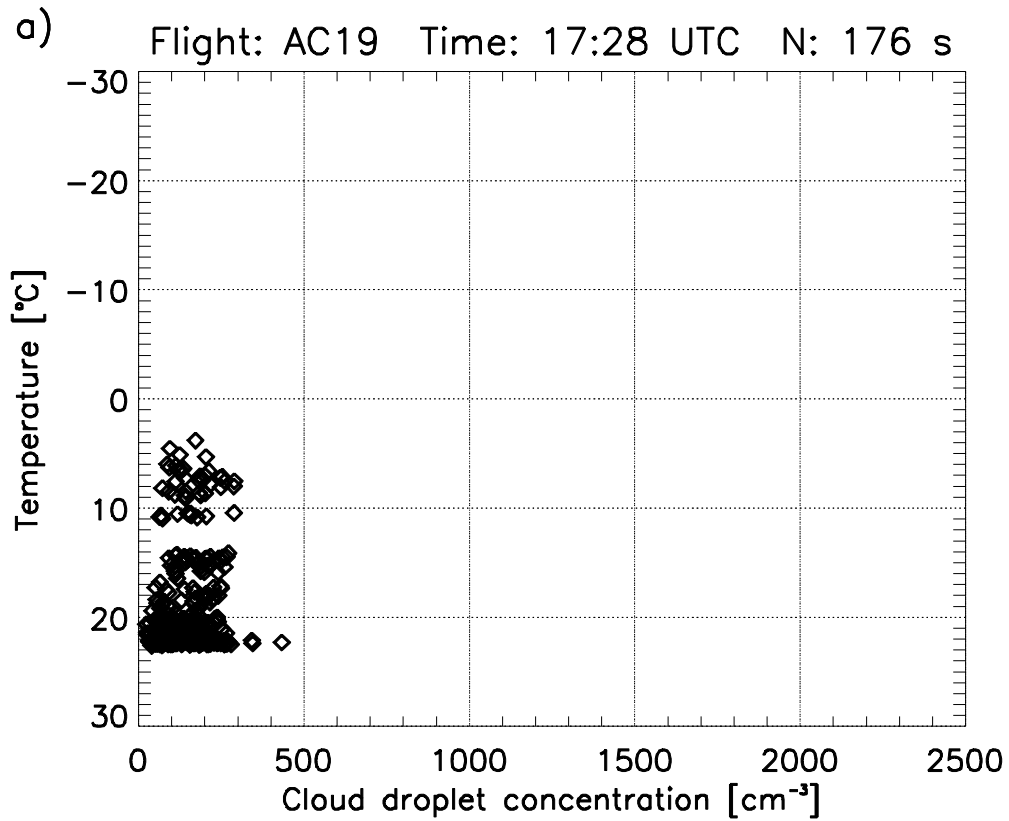
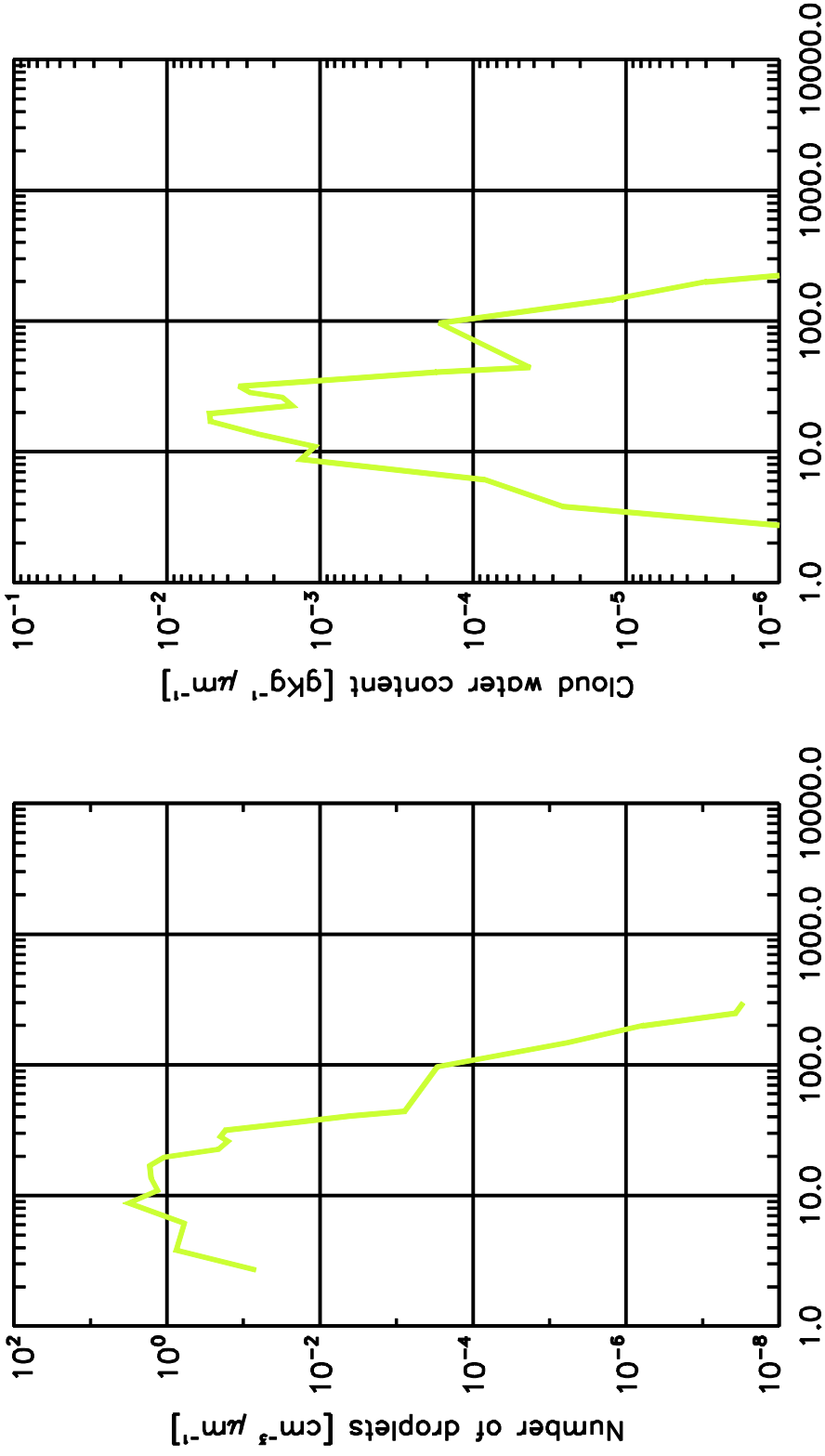
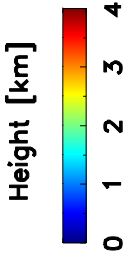


Figure 8 a) Cloud droplet concentrations measured with the CCP-CDP as a function of temperature for flight AC19. Each dot indicates 1Hz average concentration. The sample number in seconds (N) and the start time of the cloud profile are shown at the top of the panel; b) Similar to Figure 7 for flight AC19.

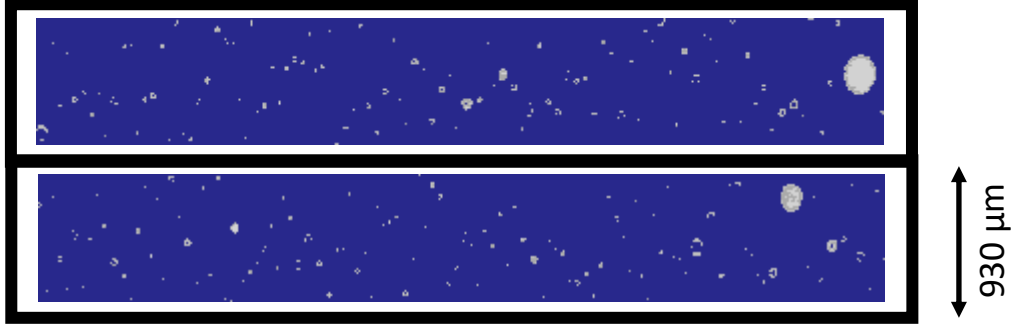
a)

Flight: AC19 Date: 2014/09/30 17:56 UTC [10 s]

H=2360 m $N_p=140 \text{ cm}^{-3}$ $DWC=0.02 \text{ gm}^{-3}$ $r_e=11.90 \text{ }\mu\text{m}$
 T=10.6 °C $CWC=0.457 \text{ gm}^{-3}$ $RWC=0.00 \text{ gm}^{-3}$



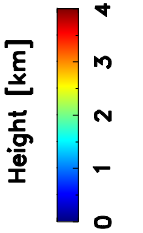
CCP-CIP Images



CCP-CDP + CCP-CIP droplet diameter [μm]

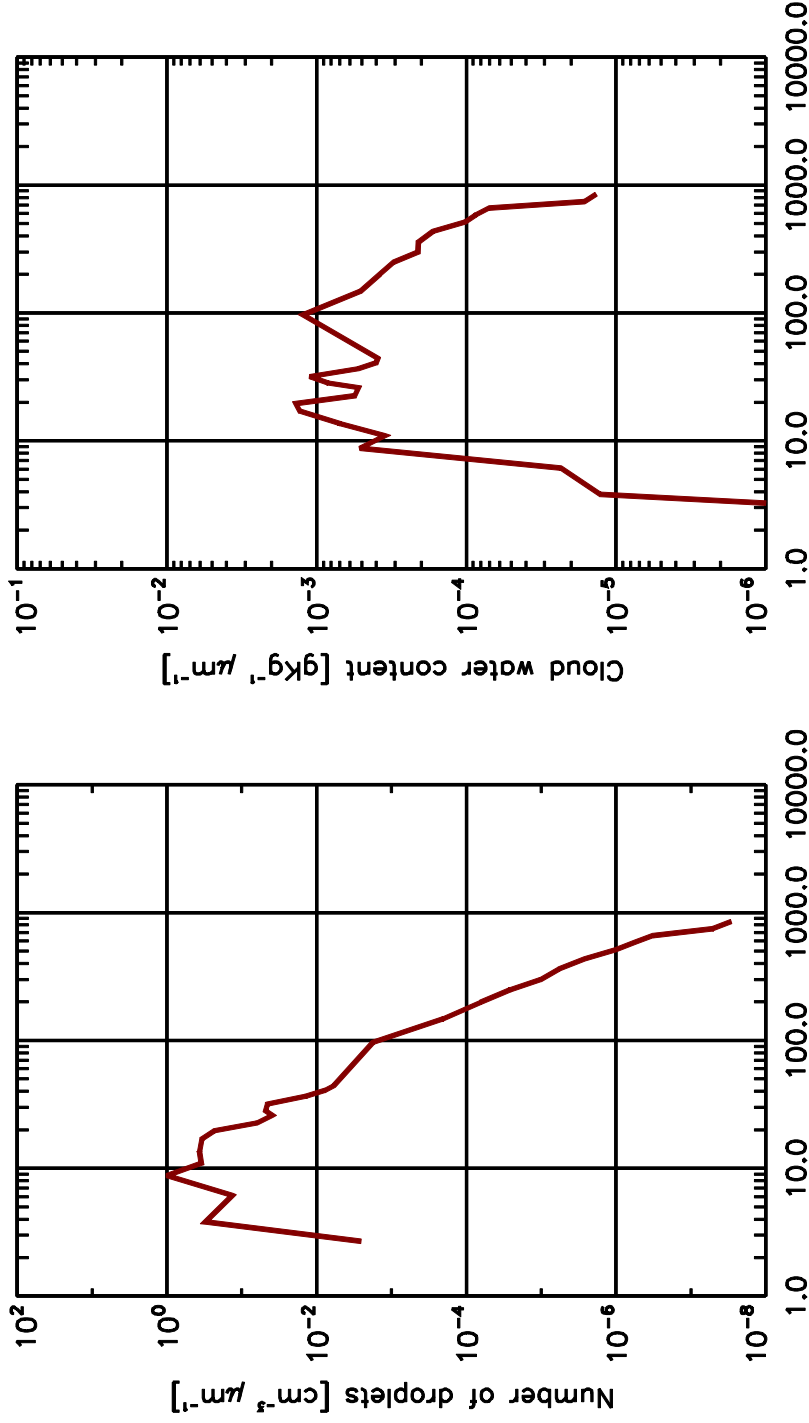
b)

Flight: AC19 Date: 2014/09/30 18:17 UTC [05 s]

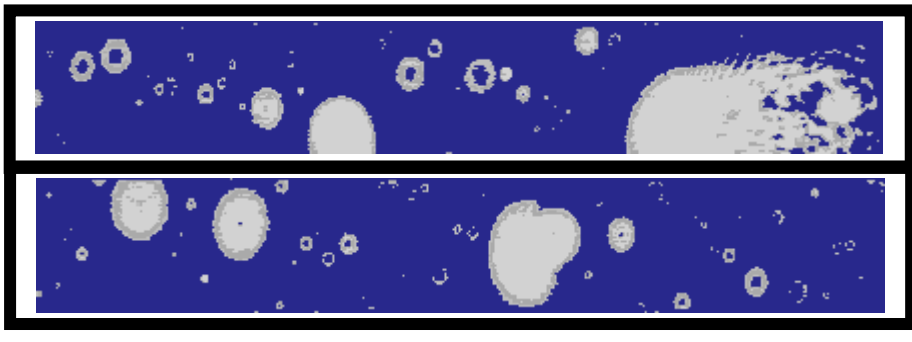


$N_p = 36 \text{ cm}^{-3}$
 $DWC = 0.24 \text{ gm}^{-3}$
 $RWC = 0.27 \text{ gm}^{-3}$

$r_e = 13.84 \text{ }\mu\text{m}$



CCP-CIP Images



930 μm

Figures 9 a-b) Similar to Figures 5a-c for flight AC19.

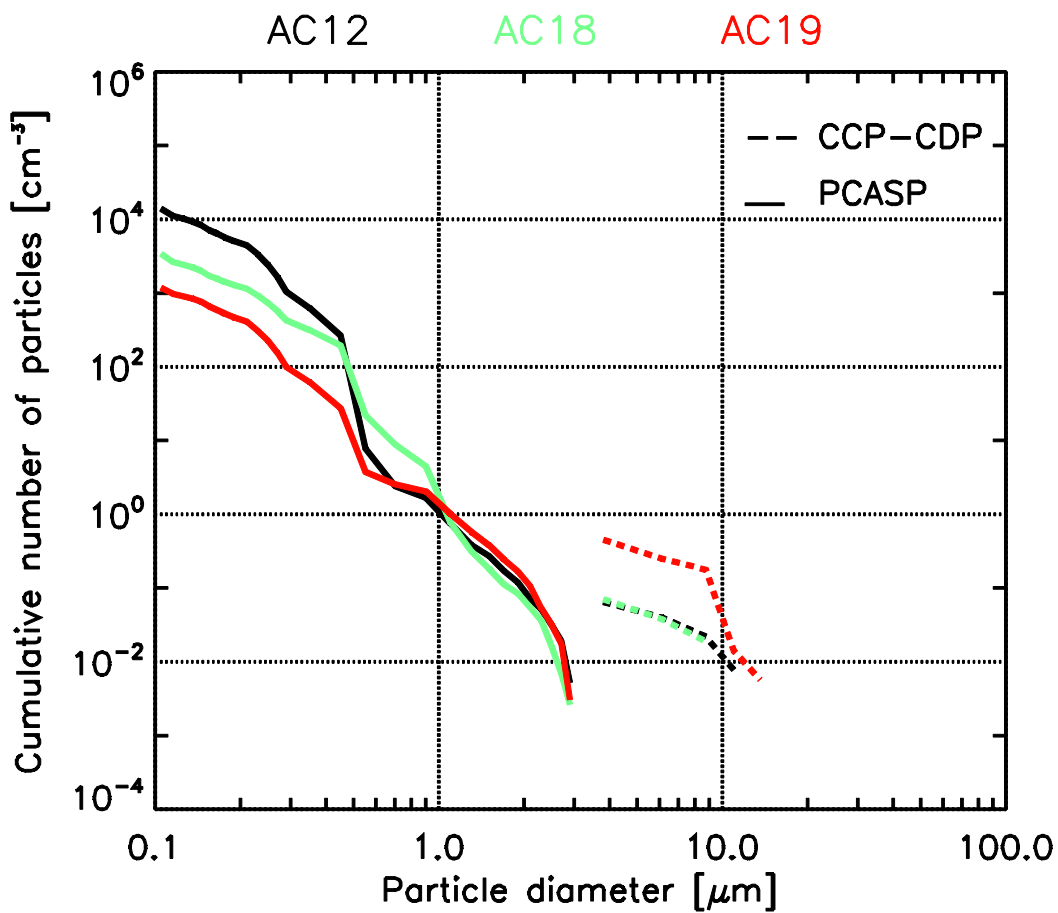


Figure 10 Cumulative aerosol size distribution below cloud base calculated from the PCASP probe for typical clean, polluted, and very polluted regions (solid line) for flights AC12 (very polluted), AC18 (polluted), and AC19 (clean). Similar for cumulative cloud droplet size distribution calculated with CCP-CDP (dashed line). The flight numbers are indicated by colors at the top of the panel.

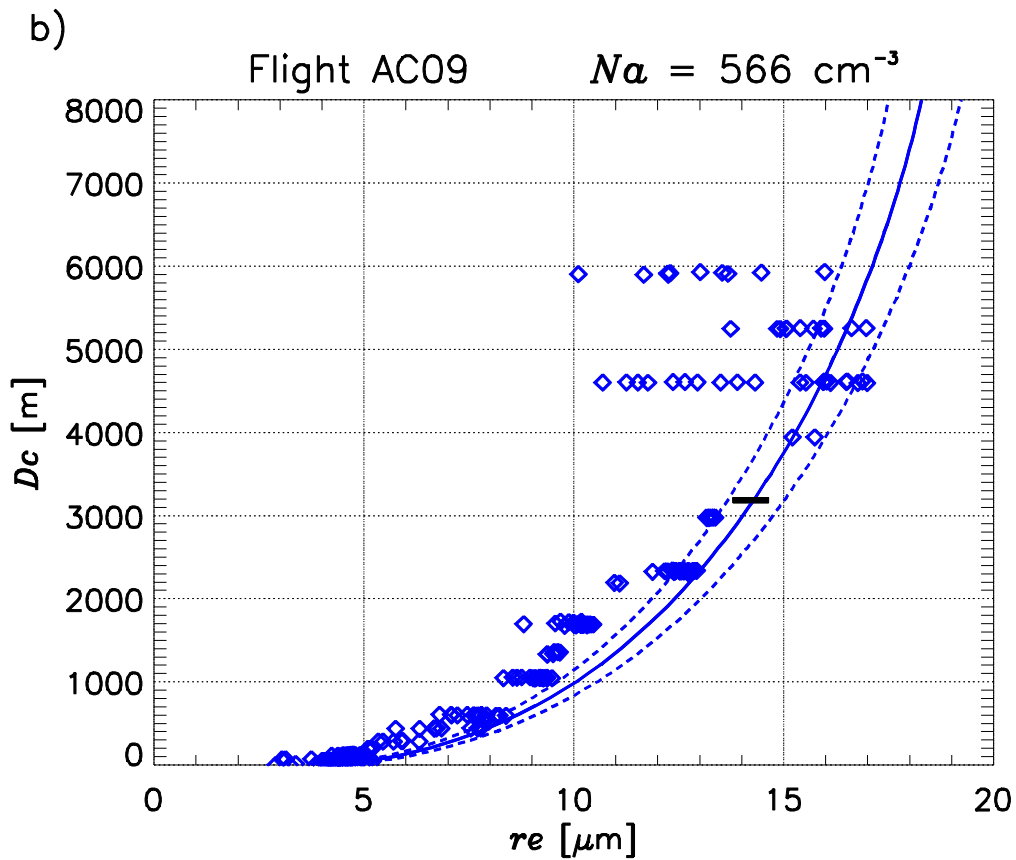
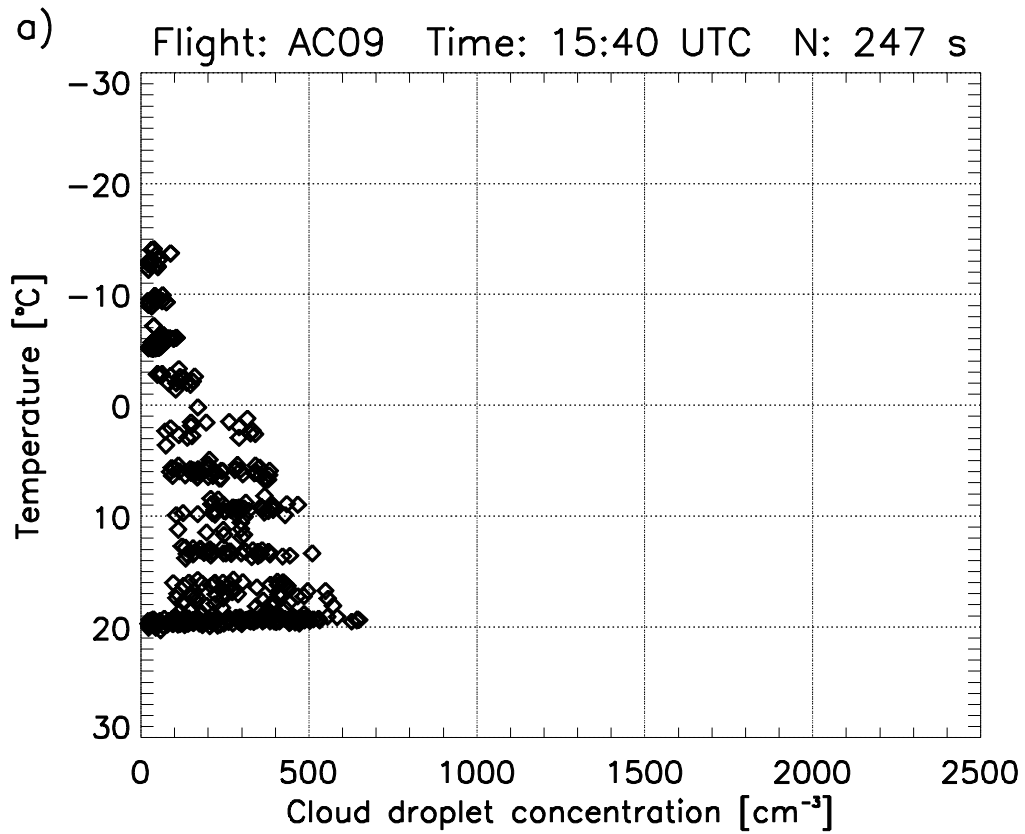


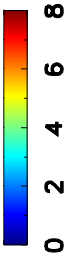
Figure 11 a) Cloud droplet concentrations measured with the CCP-CDP as a function of temperature for flight AC09. Each dot indicates 1-Hz average concentration. The sample number in seconds (N) and the start time of the cloud profile are shown at the top of the panel; b) Similar to Figure 7 for flight AC09.

a)

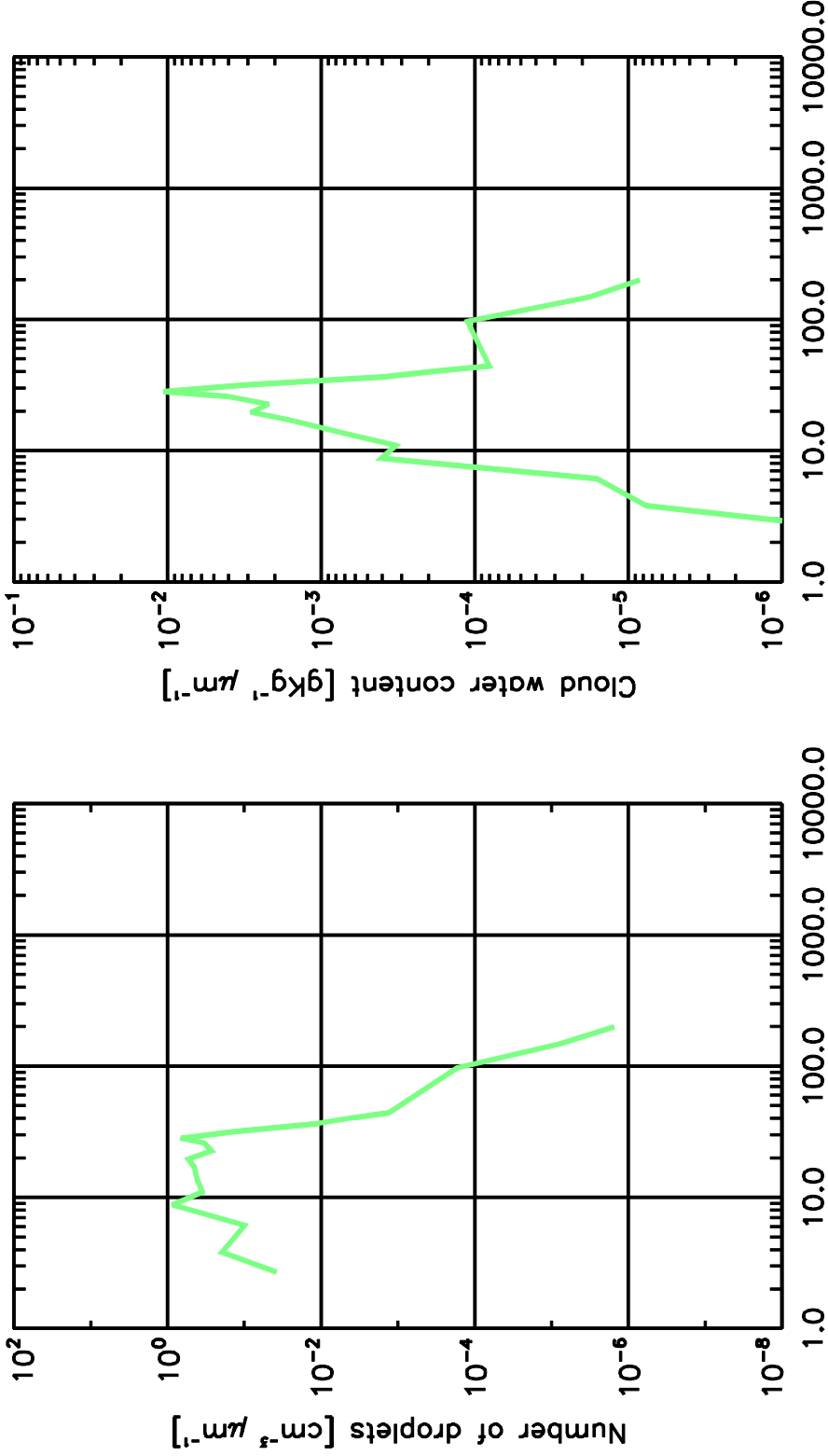
Flight: AC09 Date: 2014/09/11 16:39 UTC [05 s]

H=4094 m $N_p=74 \text{ cm}^{-3}$ $DWC=0.01 \text{ gm}^{-3}$
 T=2.4 °C $CWC=0.505 \text{ gm}^{-3}$ $RWC=0.00 \text{ gm}^{-3}$

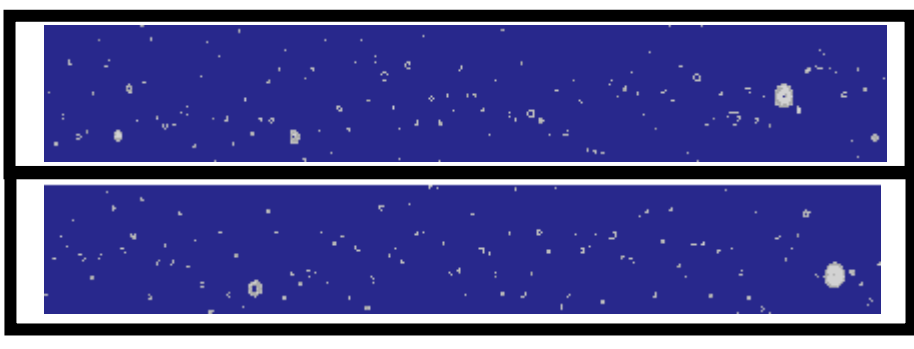
Height [km]



$r_e=13.42 \mu\text{m}$



CCP-CIP Images



930 μm

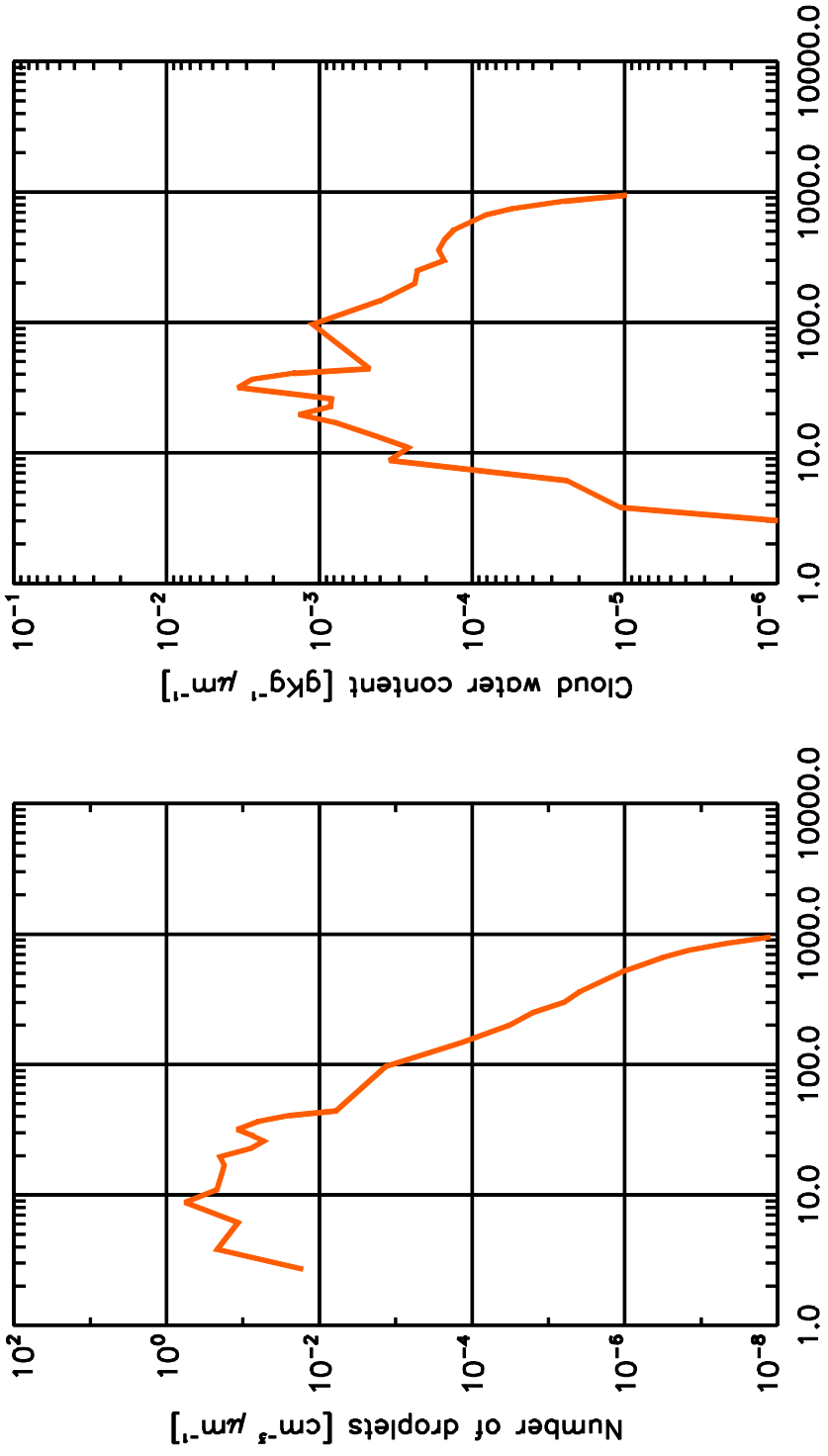
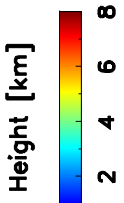


CCP-CDP + CCP-CIP droplet diameter [μm]

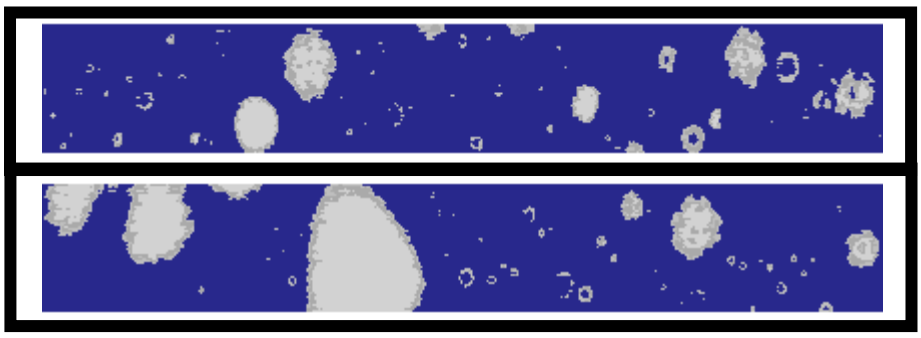
b)

Flight: AC09 Date: 2014/09/11 17:13 UTC [04 s]

H=6417 m $N_p=31 \text{ cm}^{-3}$ $DWC=0.16 \text{ gm}^{-3}$ $r_e=15.97 \text{ }\mu\text{m}$
 T=-9.2 °C $CWC=0.247 \text{ gm}^{-3}$ $RWC=0.27 \text{ gm}^{-3}$



CCP-CIP Images



930 μm

CCP-CDP + CCP-CIP droplet diameter [μm]

Figures 12 a-b) Similar to Figures 5a-c for flight AC09.

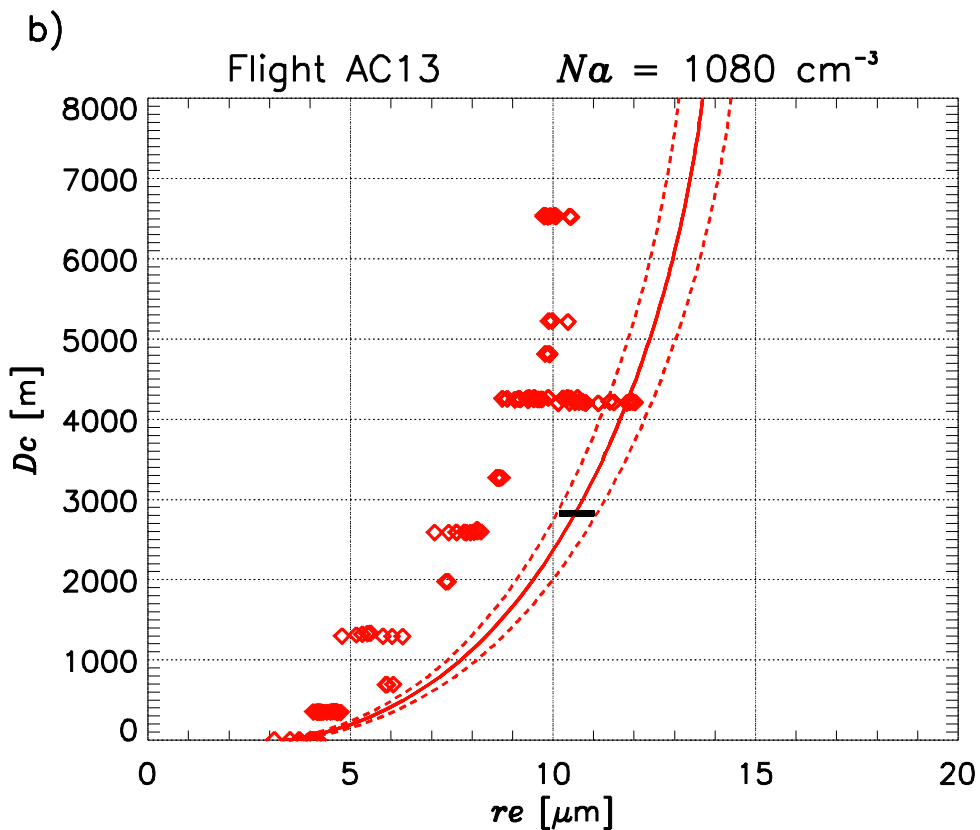
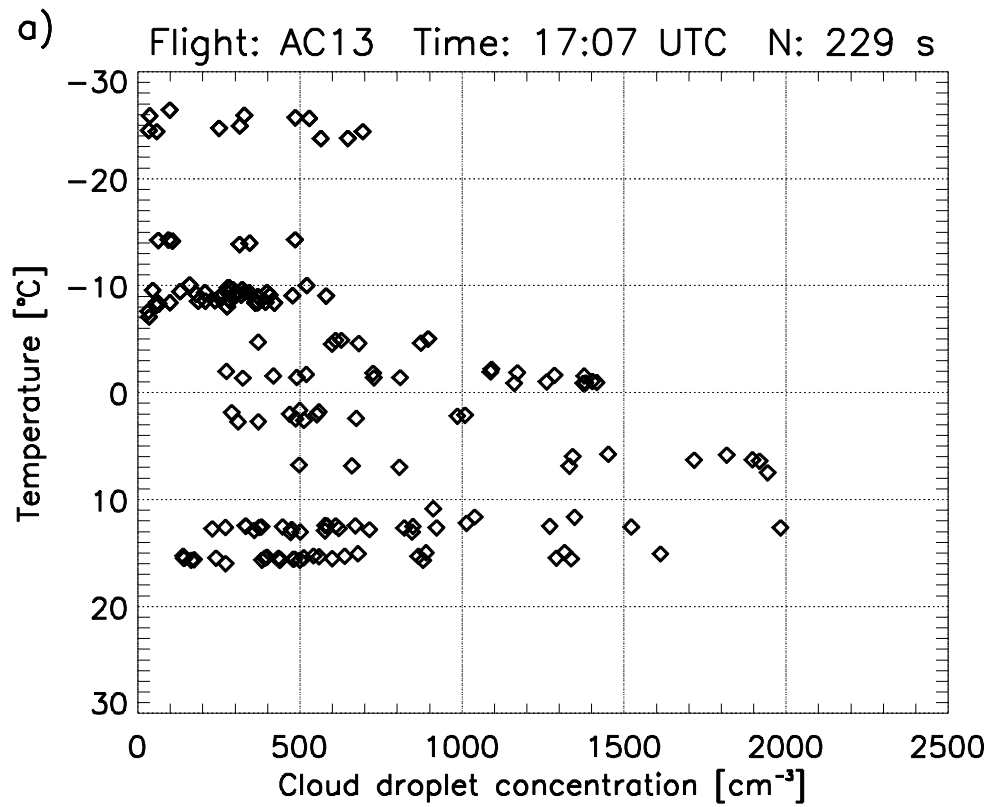
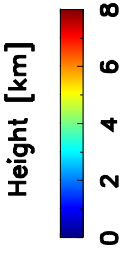


Figure 13 a) Cloud droplet concentration measured with the CCP-CDP probe as a function of temperature for flight AC13. Each dot indicates a 1-Hz average concentration. The sample number and the approximate time of the cloud profile are shown at the top of the panel; b) Similar to Figure 7 for Flight AC13.

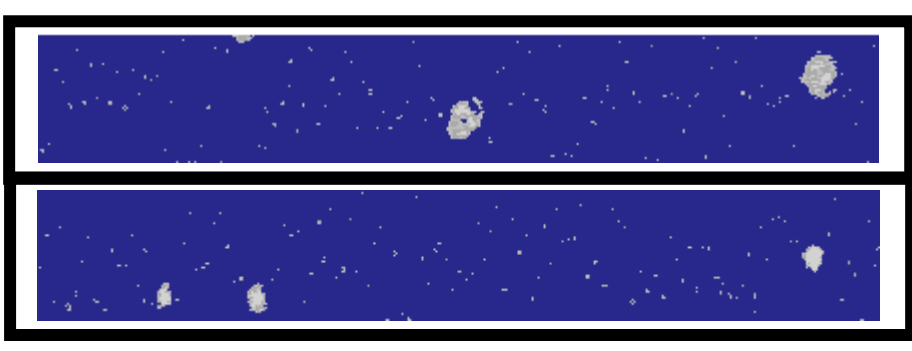
Flight: AC13 Date: 2014/09/19 18:28 UTC [03 s]

H=7008 m
T=-14.1 °C
N_p=380 cm⁻³
CWC=1.348 gm⁻³

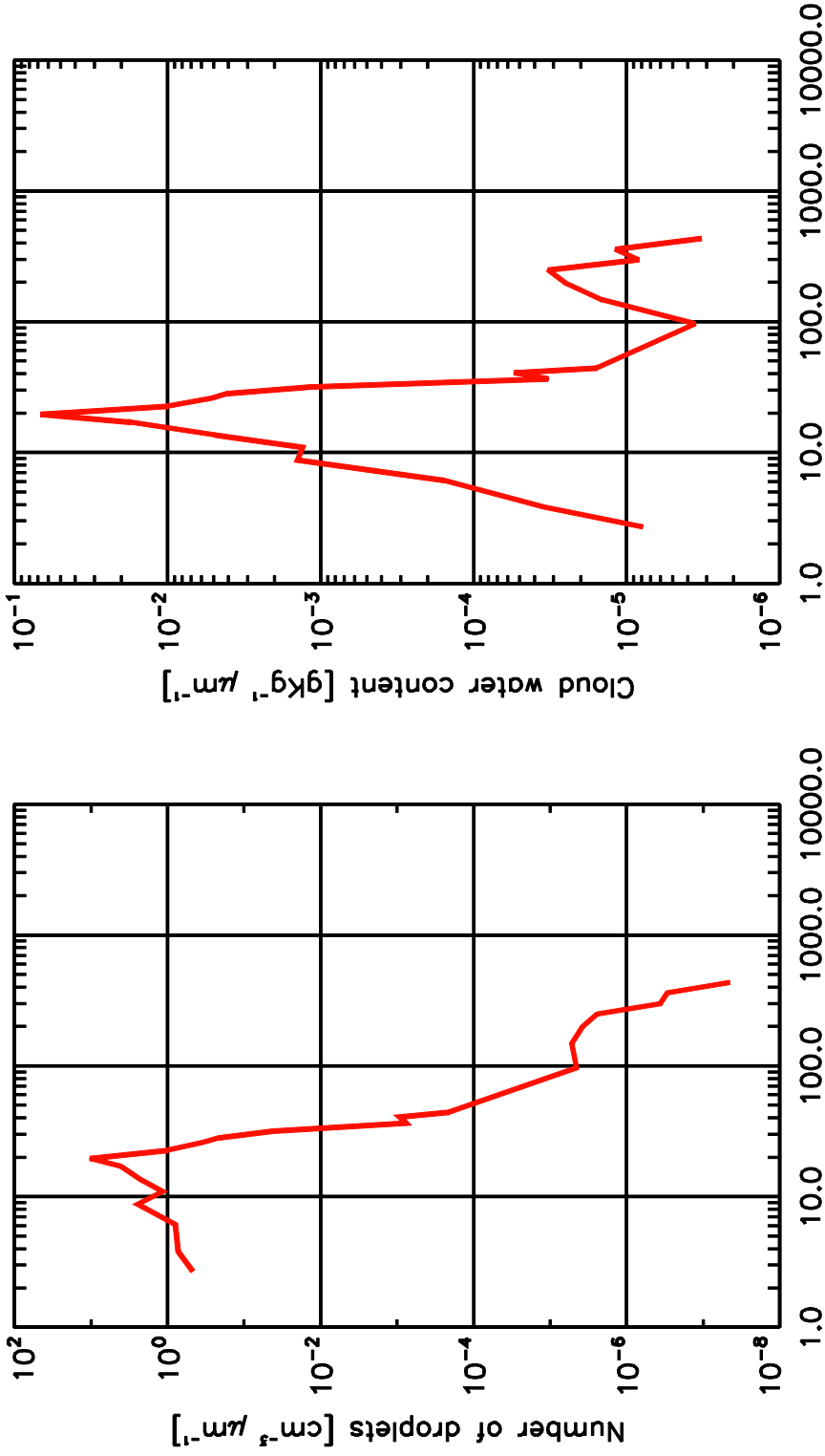
DWC=0.01 gm⁻³
RWC=0.00 gm⁻³



CCP-CIP Images



930 μm



Figures 14 Similar to Figures 5a-c for flight AC13.

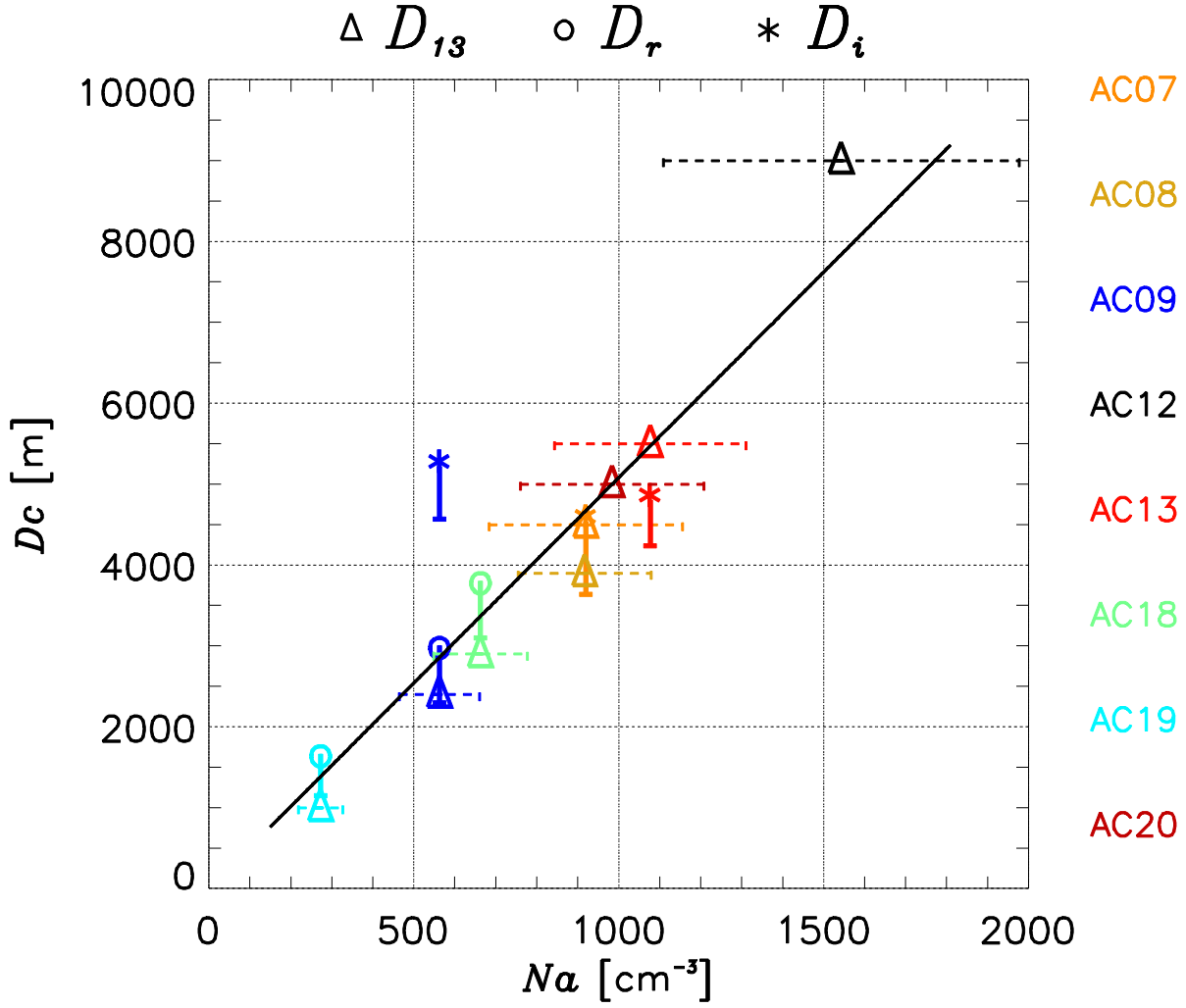


Figure 15 Cloud depth (D_c) as a function of the estimated adiabatic number of droplets (N_a) at cloud base. D_c for adiabatic cloud droplet effective radius (r_{ea}) equal $13 \mu\text{m}$ (or D_{13}) are indicated by triangles. Similar for cloud depth of rain initiation (D_r) [indicated by circles] and cloud depth for ice initiation (D_i) [indicated by asterisk]. The flight numbers are indicated by colors on the right side of the panel. The values of D_{13} , D_r , and D_i are shown in Table 1. The uncertainties of N_a estimates are shown by horizontal error bars. The vertical error bars indicate the cloud depth between D_r and D_{r-1} or D_i and D_{i-1} . The black line indicates the linear equation for D_{13} as a function of N_a for all flights, where: $D_r = (5 \pm 1.06)N_a$.

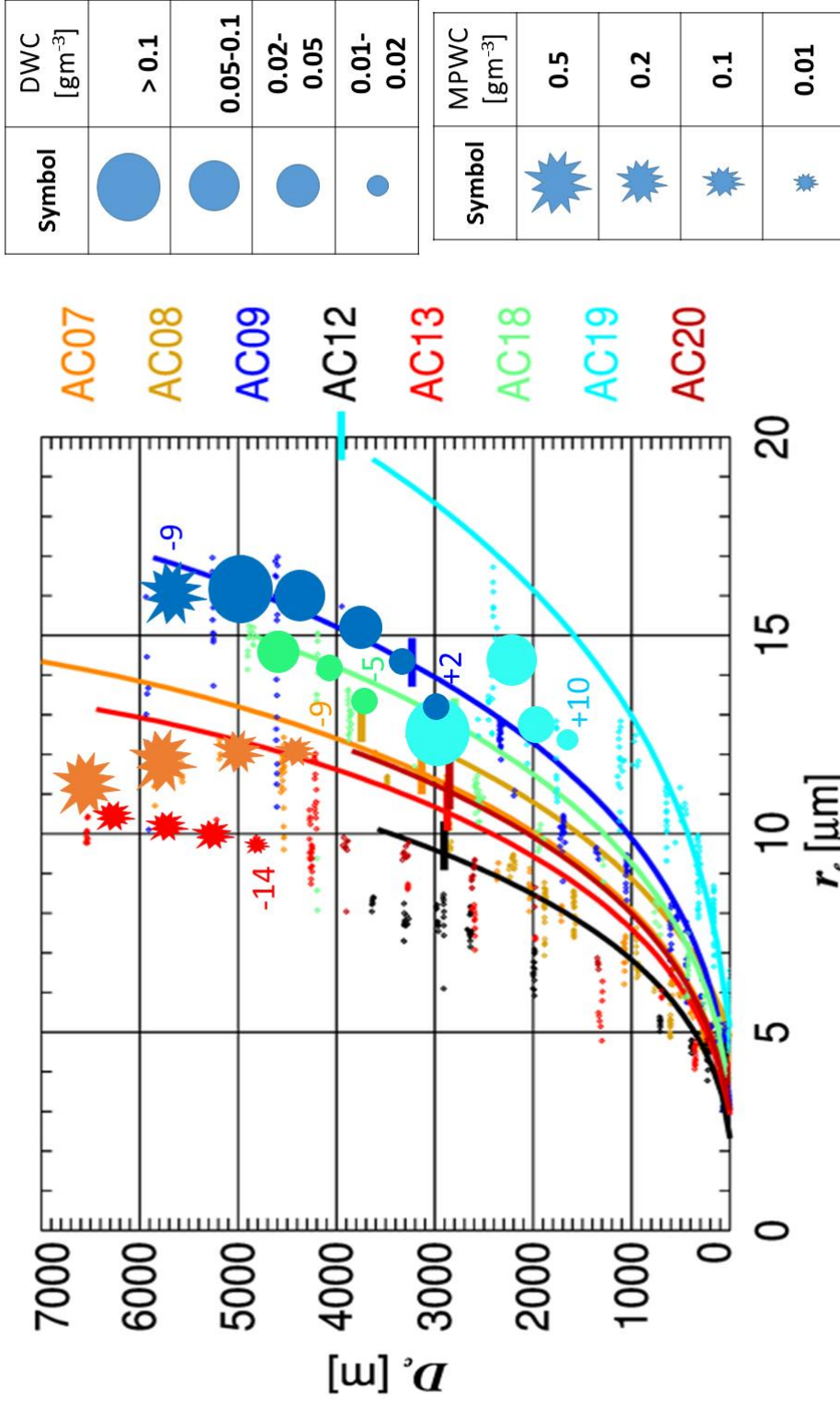


Figure 16 CDP-measured cloud droplet effective radius (r_e) (colored dots) and estimated cloud droplet adiabatic effective radius (r_{ea}) (colored lines) as a function of cloud depth (D_c) for all flights (indicated by colors). The height of 0 °C is indicated by a horizontal bar across the r_{ea} line. The circles indicate the approximate values of drizzle water content (DWC) calculated from the CCP-CIP data, the range of DWC values is indicated in the table at the upper-right side of the figure. The star symbols indicate approximate mixed phase drizzle water content (MPWC) values calculated from the CCP-CIP data (indicated in the table at the bottom-right side of the figure). The temperature in °C of rain or ice initiation (D_r and D_i , respectively) is indicated by colored numbers close to the circle or star symbols.

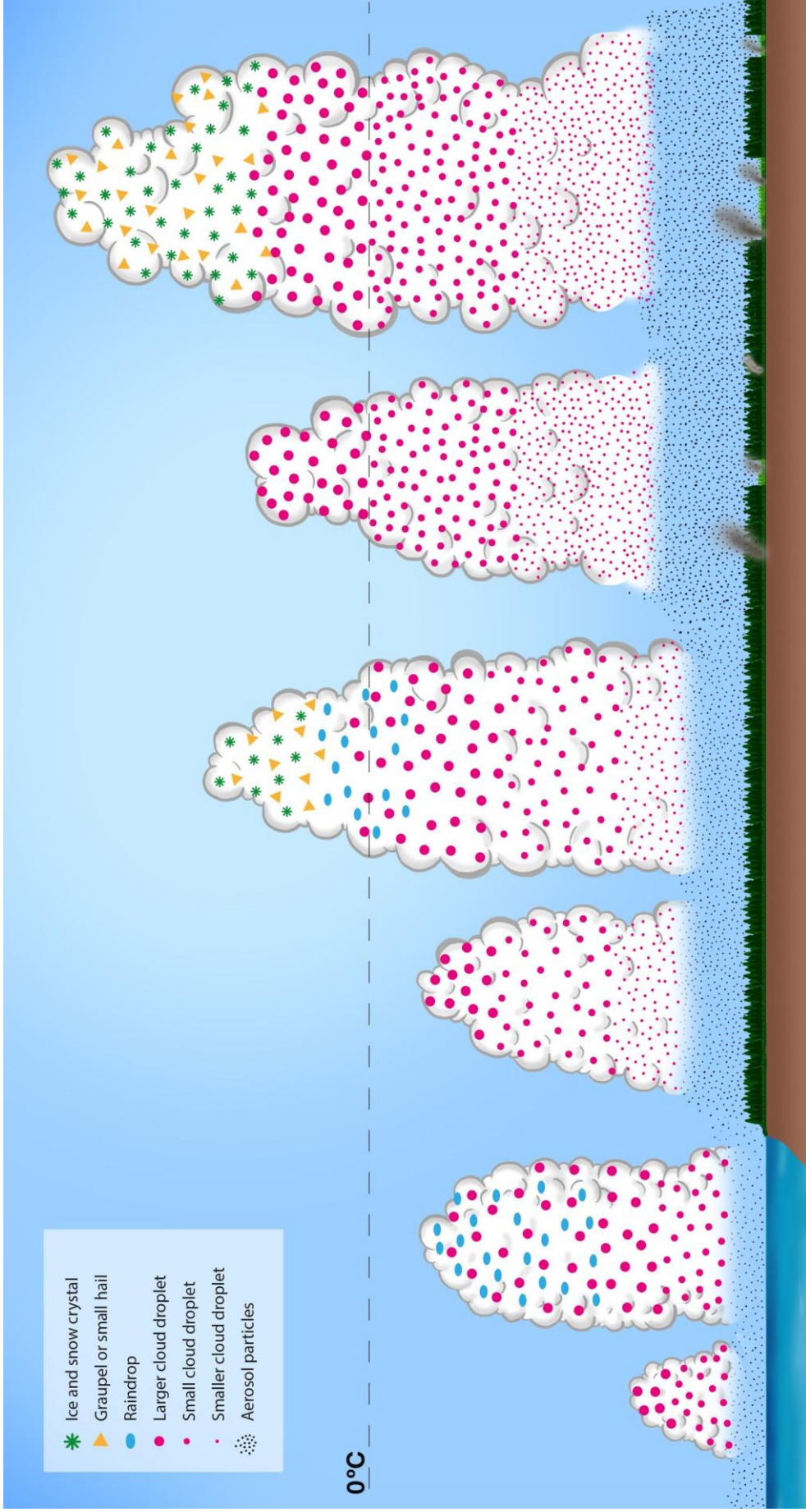


Figure 17. General characteristics of growing convective cumulus formed over the Amazon basin during the dry season. The heights of cloud base are higher over continental Amazon due to the smaller relative humidity in comparison with the maritime region. Convective clouds formed over the Atlantic Ocean, near the Brazilian coast, have smaller cloud droplets concentration (N_d) at cloud base due to the smaller concentration of aerosol and updraft speeds below cloud base. The initiation of warm rain (D_r) is observed at lower cloud depths (~ 2 km or $\sim 10^\circ\text{C}$) from collision and coalescence processes. When convective clouds are more continental, larger aerosol concentration and updrafts are observed below cloud base, leading to larger N_d nucleated at cloud base (as observed above forested and deforested regions). Over the forest D_r is observed near 0°C , whilst for the deforestation are region the collision and coalescence processes are totally suppressed and the formation of ice particles took place at higher altitudes in the clouds in very polluted conditions, because the resulting smaller cloud droplets froze at colder temperatures compared to the larger drops in the less polluted cases.